Isospin-dependent multifragmentation of relativistic projectiles

R. Ogul,[1,2] A. S. Botvina,[1,3] U. Atav,[2] N. Buyukcizmeci,[2] I. N. Mishustin,[4,5] P. Adrich,[1] T. Aumann,[1] C. O. Bacri,[6] T. Barczyk,[7] R. Bassini,[8] S. Bianchin,[1] C. Boiano,[8] A. Boudard,[9] J. Brzychczyk,[7] A. Chbihi,[10] J. Cibor,[11] B. Czech,[11] M. De Napoli,[12] J.-É. Ducret,[9] H. Emling,[1] J. D. Frankland,[10] M. Hellström,[1] D. Henzlova,[1] G. Immè,[12] I. Iori,[8,*] H. Johansson,[1] K. Kezzar,[1] A. Lafriakh,[9] A. Le Fèvre,[1] E. Le Gentil,[9] Y. Leifels,[1] J. Lühning,[1] J. Łukasik,[1,11] W. G. Lynch,[13] U. Lynen,[1] Z. Majka,[7] M. Mocko,[13] W. F. J. Müller,[1] A. Mykulyak,[14] H. Orth,[1] A. N. Otte,[1] R. Palit,[1] P. Pawłowski,[11] A. Pullia,[8] G. Raciti,[12,*] E. Rapisarda,[12] H. Sann,[1,*] C. Schwarz,[1] C. Sfienti,[1] H. Simon,[1] K. Sümmerer,[1] W. Trautmann,[1] M. B. Tsang,[13] G. Verde,[13] C. Volant,[9] M. Wallace,[13] H. Weick,[1] J. Wiechula,[1] A. Wieloch,[7] and B. Zwiegliński[14]

[1]*GSI Helmholtzzentrum für Schwerionenforschung GmbH, D-64291 Darmstadt, Germany*
[2]*Department of Physics, University of Selçuk, TR-42079 Konya, Turkey*
[3]*Institute for Nuclear Research, Russian Academy of Sciences, RU-117312 Moscow, Russia*
[4]*Frankfurt Institute for Advanced Studies, J.W. Goethe University, D-60438 Frankfurt am Main, Germany*
[5]*Kurchatov Institute, Russian Research Center, RU-123182 Moscow, Russia*
[6]*Institut de Physique Nucléaire, IN2P3-CNRS et Université, F-91406 Orsay, France*
[7]*M. Smoluchowski Institute of Physics, Jagiellonian University, PL-30059 Kraków, Poland*
[8]*Istituto di Scienze Fisiche, Università degli Studi and INFN, I-20133 Milano, Italy*
[9]*DAPNIA/SPhN, CEA/Saclay, F-91191 Gif-sur-Yvette, France*
[10]*GANIL, CEA et IN2P3-CNRS, F-14076 Caen, France*
[11]*H. Niewodniczański Institute of Nuclear Physics, PL-31342 Kraków, Poland*
[12]*Dipartimento di Fisica e Astronomia-Università and INFN-Sezione CT and LNS, I-95123 Catania, Italy*
[13]*Department of Physics and Astronomy and NSCL, Michigan State University, East Lansing, Michigan 48824, USA*
[14]*A. Sołtan Institute for Nuclear Studies, PL-00681 Warsaw, Poland*

(Received 4 June 2010; published 24 February 2011)

The N/Z dependence of projectile fragmentation at relativistic energies has been studied with the ALADIN forward spectrometer at the GSI Schwerionen Synchrotron (SIS). Stable and radioactive Sn and La beams with an incident energy of 600 MeV per nucleon have been used in order to explore a wide range of isotopic compositions. For the interpretation of the data, calculations with the statistical multifragmentation model for a properly chosen ensemble of excited sources were performed. The parameters of the ensemble, representing the variety of excited spectator nuclei expected in a participant-spectator scenario, are determined empirically by searching for an optimum reproduction of the measured fragment-charge distributions and correlations. An overall very good agreement is obtained. The possible modification of the liquid-drop parameters of the fragment description in the hot freeze-out environment is studied, and a significant reduction of the symmetry-term coefficient is found necessary to reproduce the mean neutron-to-proton ratios $\langle N\rangle/Z$ and the isoscaling parameters of $Z \leqslant 10$ fragments. The calculations are, furthermore, used to address open questions regarding the modification of the surface-term coefficient at freeze-out, the N/Z dependence of the nuclear caloric curve, and the isotopic evolution of the spectator system between its formation during the initial cascade stage of the reaction and its subsequent breakup.

DOI: 10.1103/PhysRevC.83.024608 PACS number(s): 25.70.Pq, 25.70.Mn, 21.65.Ef

I. INTRODUCTION

Multifragmentation is a universal phenomenon occurring when a large amount of energy is deposited in a nucleus. It has been observed in nearly all types of high-energy nuclear reactions induced by hadrons, photons, and heavy ions (for reviews, see Refs. [1–4]). At low excitation energies, the produced nuclear system can be treated as a compound nucleus [5] which decays via evaporation of light particles or fission. However, at high excitation energy, possibly accompanied by compression during the initial dynamical stage of the reaction [6–8], the system will expand to subsaturation densities, thereby becoming unstable, and will break up into many fragments.

Multifragmentation has been shown to be a fast process with characteristic times around 100 fm/c or less (see, e.g., Refs. [9–11]). Nevertheless, as evident from numerous analyses of experimental data, a high degree of equilibration can be reached in these reactions. In particular, chemical equilibrium among the produced fragments is very likely while kinetic equilibration may not be reached [12]. Statistical models were found very suitable for describing the measured fragment yields [1,2,13–19]. Even though equilibration may not occur within the individual system during the primary reaction stage the processes are, apparently, of such complexity that dynamical constraints beyond the conservation laws do not restrict the statistical population of the available partition space.

Taking multifragmentation into account is crucially important for a correct description of fragment production in high-energy reactions. Depending on the chosen projectile,

*Deceased.

it is responsible for 10 to 50% of the reaction cross section. Multifragmentation, furthermore, opens a unique possibility for investigating the phase diagram of nuclear matter at temperatures $T \approx 3$–8 MeV and densities around $\rho \approx 0.1\rho_0$–$0.3\rho_0$ ($\rho_0 \approx 0.15$ fm^{-3} denotes the nuclear saturation density). These equilibrium conditions coincide with those of the nuclear liquid-gas coexistence region. Very similar conditions are realized in stellar matter during the expansion phase of supernova explosions [20–22]. The study of multifragmentation thus receives a strong astrophysical motivation from its relation to stellar evolution and the formation of nuclei, occurring at densities near or below ρ_0 and over a wide range of isotopic asymmetries. The characteristics of multifragmentation as a function of the neutron-to-proton ratio N/Z of the disintegrating system are, therefore, of particular interest.

Previous ALADIN experimental data have provided extensive information on charged fragment production in multifragmentation reactions [23,24]. In particular, they have demonstrated a "rise and fall" of multifragmentation with excitation energy [25,26], and they have shown that the temperature remains nearly constant, around $T \sim 6$ MeV, during this process [12,27,28], as predicted within the statistical approach [29]. The observed large fluctuations of the fragment multiplicity and of the size of the largest fragment in the transition region from a compoundlike decay to multifragmentation have been interpreted as manifestations of the nuclear liquid-gas phase transition in small systems (see, e.g., Refs. [16,30–32] and references given therein).

In this article, the study of multifragmentation is extended to isotopic effects. New data for projectile fragmentation at 600 MeV/nucleon are presented together with their statistical analysis within the framework of the statistical multifragmentation model [2]. The data were obtained during the ALADIN experiment S254 [33–35] in which a maximum range in N/Z was explored by using primary stable beams as well as secondary radioactive beams, up to the presently achievable limit on the neutron-poor side. The projectile isotopic compositions are expected to be essentially preserved during the initial stages of the collision, so that the study can fully benefit from the asymmetry of available secondary beams.

The mass of the produced spectator systems varies considerably with the impact parameter and is closely linked to the transferred excitation energy. The theoretical analysis is, therefore, based on calculations for a full ensemble of spectator systems intended to reflect these properties of spectator fragmentation. The parameters describing the ensemble of excited nuclei are chosen to obtain a best possible reproduction for a set of experimental observables. We concentrate on observables describing the partition degrees of freedom and on the information they carry regarding the fragment properties at the chemical freeze-out. It is shown that a very satisfactory description of the N/Z dependence of multifragmentation can be obtained within the statistical framework, including that of the freeze-out temperatures [35]. The reduction of the symmetry term coefficient in the low-density freeze-out environment, reported for ^{12}C-induced reactions on ^{112,124}Sn isotopes [36], is confirmed and found necessary to reproduce the measured mean neutron-to-proton ratios $\langle N\rangle/Z$ and the isoscaling parameters of intermediate-mass fragments.

II. EXPERIMENTAL DETAILS

The ALADIN experiment S254, conducted in 2003 at the GSI Schwerionen Synchrotron (SIS), was designed to study isotopic effects in projectile fragmentation at relativistic energies. Besides stable ^{124}Sn, neutron-poor secondary Sn and La beams were used to extend the range of isotopic compositions beyond that available with stable beams alone. The radioactive secondary beams were produced at the fragment separator (FRS) [37] by the fragmentation of primary ^{142}Nd projectiles of about 900 MeV/nucleon in a thick beryllium target. The FRS was set to select ^{124}La and, in a second part of the experiment, also ^{107}Sn projectiles which were then delivered to the ALADIN experimental setup. All beams had a laboratory energy of 600 MeV/nucleon and were directed onto reaction targets consisting of $^{\text{nat}}$Sn with areal density 500 or 1000 mg/cm^2.

For the runs with secondary beams, to reach the necessary beam intensity of about 10^3 particles/s with the smallest possible mass-to-charge ratio A/Z, it was found necessary to accept a distribution of neighboring nuclides together with the requested ^{124}La or ^{107}Sn isotopes. The mean compositions of the nominal ^{124}La (^{107}Sn) beams were $\langle Z\rangle = 56.8$ (49.7) and $\langle A/Z\rangle = 2.19$ (2.16), respectively [38]. Model studies confirm that these $\langle A/Z\rangle$ values are also representative for the spectator systems emerging after the initial stages of the reaction [36,39].

The ALADIN experimental setup has been described previously [24]. For the present experiment, it has been upgraded by constructing a new set of eight proportional readout chambers for the TP-MUSIC IV detector and by a redesign of all components of the electronic readout chain [40]. Digitization of the linear signals was performed with the aid of 40-MHz sampling ADC's right after the preamplifier stage, permitting digital filtering and background suppression. The readout planes on either side of the TP-MUSIC IV chamber were divided into four proportional-counter sections and three ionization-anode sections. Each section extended over the full height of the chamber, and proportional and ionization sections alternated along the beam direction. With this arrangement, either type of detector could be used to record the fragment trajectories. Their horizontal coordinates, i.e., in the bending plane of the magnet, were obtained from the measured drift times while the vertical coordinates were determined from the positions along the proportional counters measured with a combination of charge-division and pad-readout techniques.

The threshold for fragment detection and identification was below atomic number $Z = 2$, obtained with the proportional counters. The threshold of the ionization sections was higher but they provided a superior Z resolution for $Z > 9$. Overall, the resolution $\Delta Z \leqslant 0.6$ (full width at half maximum) of the full detector was nearly independent of Z up to the projectile Z and permitted the individual identification of detected fragments according to their atomic number Z. Examples of recorded inclusive Z spectra for the cases of stable ^{124}Sn projectiles and radioactive ^{107}Sn (nominal) projectiles

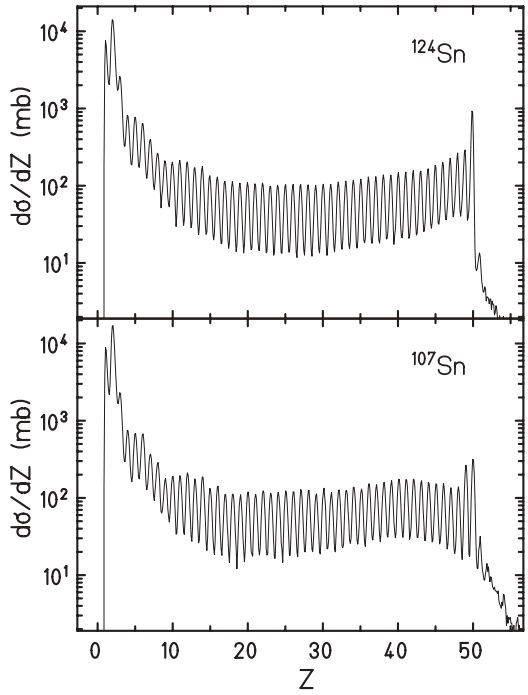

FIG. 1. Measured cross section as a function of the fragment atomic number Z determined with the TP-MUSIC IV detector for ^{124}Sn (top panel) and ^{107}Sn projectiles (bottom panel). Note that the experimental trigger conditions affected the yields for $Z > 40$.

are shown in Fig. 1. They are given on an absolute scale but the recorded cross sections for very large fragments (about $Z > 40$) are underestimated due to inefficiencies of the experimental trigger as discussed further below. The figure also shows that all elements are produced in multifragmentation reactions with an intensity that varies rather smoothly with Z. For ^{124}Sn, the recorded inclusive cross section for the production of fragments with $3 \leqslant Z \leqslant 49$ is 5.9 b. Charge pickup to $Z = 51$ appears with 8 mb in the spectrum, a value fitting well into the systematics collected for this process [41]. Very similar cross sections were obtained for ^{107}Sn projectiles. The most significant difference is the lower intensity near the atomic number of the projectile in the case of ^{107}Sn, following from the reduced probability for neutron evaporation of neutron-poor heavy residue nuclei (see below). Traces of the neighboring nuclides in the nominal ^{107}Sn beams are visible around $Z = 50$. Smaller differences are observed in the range $Z < 20$ where the odd-even Z staggering is slightly more pronounced, on the level of 10%, in the ^{107}Sn case.

The magnetic rigidities of detected fragments were determined by backtracing their trajectories through the magnetic field region of the ALADIN magnet, starting from the vectors determined with the TP-MUSIC IV detector. With an iterative procedure, the rigidity was varied until the calculated trajectory coincided with the measured coordinates of the projectile in the target plane, perpendicular to the beam direction. A thin plastic detector of 200 μm in thickness, positioned close to the target and viewed by photomultipliers at four sides, was used for this purpose. The achieved position resolution amounted to ≈1.5 mm, horizontally and vertically, over the active area of 4×4 cm^2 chosen for the secondary beam experiments.

The fragments, with velocities of approximately that of the projectile, can be assumed to be fully stripped of all electrons [42]. Fragment momenta were determined from the measured rigidities and atomic numbers Z and used to determine fragment masses by including the time-of-flight information given by the ALADIN time-of-flight wall [24]. The obtained time-of-flight resolution varied with Z, smoothly decreasing from ≈250 ps (standard deviation) for lithium fragments to ≈100 ps for fragments with $Z \geqslant 10$. The start time was derived from the projectile arrival time measured with a second thin plastic foil of 75 μm in thickness, mounted upstream at an angle of 45° with respect to the beam direction and viewed by two photomultiplier tubes. The resolution obtained for the arrival time was ≈30 ps (standard deviation).

The obtained mass resolution is about 3% for fragments with $Z \leqslant 3$ (standard deviation), decreases to 1.5% for $Z \geqslant 6$, and was found to be the same in the experiments with stable and radioactive beams (Fig. 2). Masses are individually resolved for fragments with atomic number $Z \leqslant 10$. For optimum resolution, correct timing signals from both the front and the back layer of the time-of-flight wall had to be required. Background-free mass spectra, without spurious peaks due to

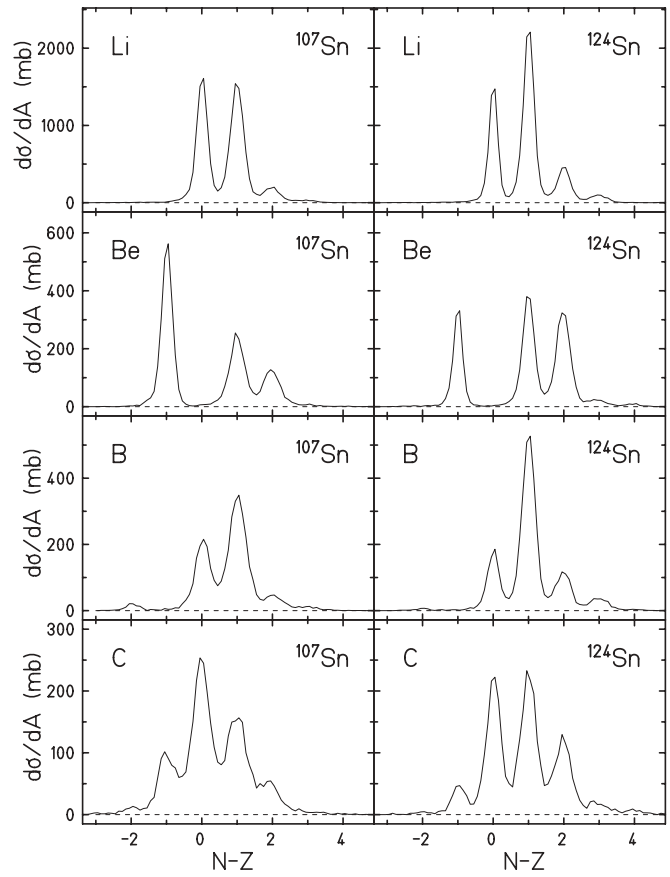

FIG. 2. Inclusive mass distributions for fragments with $3 \leqslant Z \leqslant 6$ obtained for ^{107}Sn projectiles (left panels) and ^{124}Sn projectiles (right panels).

misidentified charges, were obtained by requiring that the Z values delivered by the TP-MUSIC IV and the two layers of the time-of-flight wall all coincided within ± 0.5 units of the adopted integer value. Because of the dead zones between adjacent scintillator slats and the reduced charge resolution of the time-of-flight wall for larger Z, this condition was met by one-half to one-fourth of the fragments with $Z \leqslant 10$. The cross section distributions shown in Fig. 2 are, therefore, normalized with respect to the recorded Z yields. The significant differences of the isotope yields for neutron-poor and neutron-rich systems are evident. They are largest for the weaker but still identifiable peaks such as, e.g., ^{8}B on the neutron-poor or ^{12}Be and ^{16}C on the neutron-rich side of the spectra. Isotopically resolved production cross sections are shown and discussed in Sec. V.

The acceptance of the ALADIN forward spectrometer, in the geometry of the present experiment, was $\pm 10.2^{\circ}$ for $N = Z$ fragments with beam velocity in the horizontal direction, i.e., in the bending plane, and $\pm 4.5^{\circ}$ in vertical direction. At the beam energy of 600 MeV, this corresponded to an acceptance increasing with Z from about 90% for projectile fragments with $Z = 3$ to values exceeding 95% for $Z \geqslant 6$. These values were obtained by fitting the measured momentum distributions in transverse directions with Gaussian functions and by estimating the yields lost in the tails. Very similar acceptances have been observed in earlier experiments at the same beam energy [24].

Because of the selective coverage of the projectile-spectator decay, the quantity Z_{bound} defined as the sum of the atomic numbers Z_i of all detected fragments with $Z_i \geqslant 2$ has been chosen as the principal variable for event sorting. Z_{bound} represents approximately the charge of the primary spectator system, apart from emitted hydrogen isotopes, and is monotonically correlated with the impact parameter of the reaction [25]. The excitation energy per nucleon of the spectator system is inversely correlated with Z_{bound} [24].

Trigger signals for reactions in the target were derived from four plastic-scintillator paddles, each 5 mm thick, of 8×50 cm^2 active area, and viewed by photomultiplier tubes at both ends. They were positioned approximately 50 cm downstream from the target at angles outside the acceptance of the spectrometer. The condition that at least one of them fired was met with nearly 100% probability by events with moderate to large charged-particle multiplicities. This is demonstrated in Fig. 3 in which the rate of interaction triggers obtained in this way is compared to the expected event rate. The latter was obtained by subtracting event rates recorded with and without a reaction target from each other.

The most notable deviation from the expected rate is seen at large Z_{bound} at which the expected yields increase rapidly while the cross section recorded with the interaction trigger remains fairly flat as a function of Z_{bound}. A rise of the cross section is expected on the basis of the reaction geometry as shown in the figure. The smooth thin line represents the cross section predicted by the spherical participant-spectator model [43] for ^{107}Sn as a function of the spectator charge Z_{spect}, plotted on the same Z scale. At small Z_{bound}, the geometric prediction falls considerably below the measured yields because emitted hydrogen isotopes are not counted in Z_{bound}, but probably also

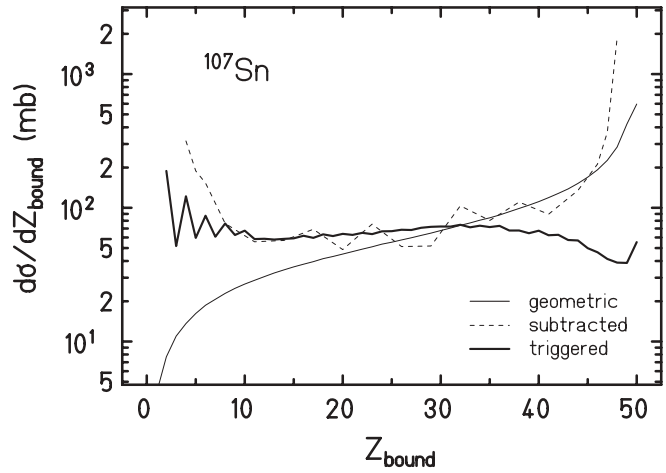

FIG. 3. Reaction cross section $d\sigma/dZ_{\mathrm{bound}}$ for ^{107}Sn projectiles as recorded with the interaction trigger (thick solid line) in comparison with the expected value obtained with the subtraction technique (dashed line, see text). The solid thin line represents, on the same abscissa, the cross section $d\sigma/dZ_{\mathrm{spect}}$ for the production of spectator nuclei with atomic number Z_{spect} according to the geometric participant-spectator model of Ref. [43].

because the sharp-edge spherical geometry is less realistic for the more central collisions.

The cross sections $d\sigma/dZ_{\mathrm{bound}}$ recorded in this way for the three cases of ^{107}Sn, ^{124}Sn, and ^{124}La projectiles are shown in Fig. 4 on a linear scale. Their integrated values of 4.3 b ($Z_{\mathrm{bound}} \leqslant 48$), 3.9 b ($Z_{\mathrm{bound}} \leqslant 49$), and 4.6 b ($Z_{\mathrm{bound}} \leqslant 55$), respectively, compare well with a calculated reaction cross section $\sigma_R = 4.8$ b ($r_0 = 1.25$ fm) for Sn + Sn collisions. It confirms that the major part of the cross section is recorded with high probability, as shown in Fig. 3. Only for very peripheral and extremely central events does a bias exist against events with small charged-particle multiplicity.

Overall, the cross sections vary rather smoothly with Z_{bound}. The drop of the cross section toward the projectile charge Z_0 in the neutron-poor cases, while it rises for ^{124}Sn, has already been noted in the Z spectra (Fig. 1) but is observed more clearly on the linear scale (Fig. 4). The fluctuations at small Z_{bound} are caused by multi-α events which enhance the even channels. The high event rates for $Z_{\mathrm{bound}} = Z_0$ are most likely due to δ electrons causing occasional spurious triggers of noninteracting projectiles.

III. STATISTICAL APPROACH TO MULTIFRAGMENTATION

A. Reaction scenario and strategy

In the scenario assumed for the statistical analysis, the multifragmentation process is subdivided into (1) a dynamical stage leading to the formation of an equilibrated nuclear system, (2) the disassembly of the system into individual primary fragments, and (3) the subsequent deexcitation of the hot primary fragments. For the description of the nonequilibrium stage of peripheral heavy-ion collisions, a variety of models can be used. Realistic calculations of ensembles

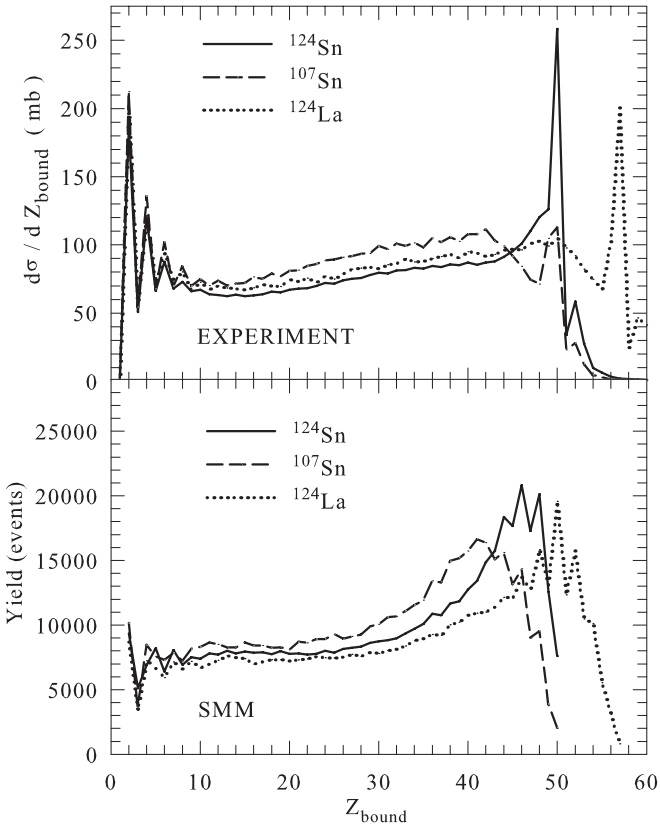

FIG. 4. Top panel: Triggered reaction cross section as a function of Z_{bound} for the three projectiles as indicated. Bottom panel: The corresponding distributions as obtained from ensemble calculations for 500 000 reaction events with standard parameters (see text).

of excited residual nuclei that undergo multifragmentation were first performed with the intranuclear cascade (INC) model [44]. More recent examples of hybrid calculations using INC or Boltzmann-Uehling-Uhlenbeck (BUU) models for the dynamical stage have been reported in Refs. [45,46].

The dynamical models agree in that the character of the dynamical evolution changes after a few rescatterings of incident nucleons, when high-energy particles ("participants") leave the system. However, the time needed for equilibration and transition to the statistical description is uncertain and model dependent [47,48]. It is estimated to be around 100 fm/c for spectator matter but the required parameters, i.e., the excitation energies, mass numbers, and charges of the predicted equilibrated sources, vary significantly even over longer times. To evade these ambiguities and other uncertainties related to the coupling with a particular dynamical model, alternative strategies have been developed [12,14,47,49–53] and are also followed here. With the results of dynamical simulations as qualitative guidelines, the exact parameters of the thermalized sources are obtained from the analysis of the experimental fragmentation data. Usually, only a subgroup of observables is required for the determination of the source parameters (see, e.g., Refs. [12,53]). The success of the statistical description is then judged from the quality of predictions for other observables and for the correlations between them.

B. Ensemble parameters

The correlations between mass and excitation energy obtained from an INC calculation [44] and of the geometric participant-spectator model [43] are shown in the top panel of Fig. 5 together with the experimental result for ^{197}Au + ^{197}Au at 600 MeV/nucleon [27]. The general correlation of an increasing excitation energy per nucleon with a decreasing mass of the produced projectile spectators is a feature common to all cases but the values differ considerably. The increase in surface energy, solely considered in the geometric model, is much smaller than the transferred energies predicted by the INC or obtained from the experiment. The latter two results are fairly consistent with each other but the excitation energies were found to be larger than what is needed for satisfactory

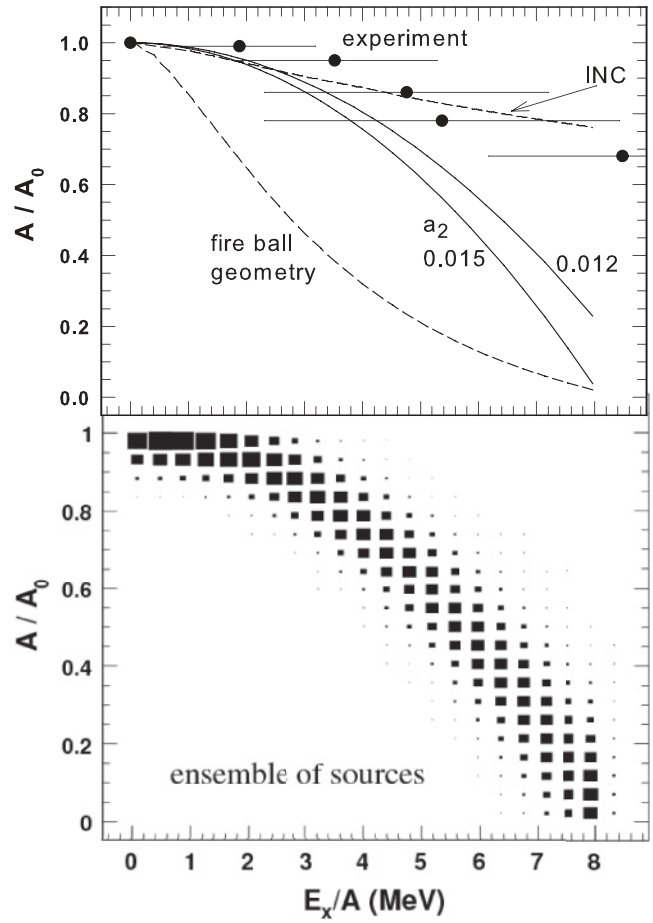

FIG. 5. Top panel: Mean reduced mass number A/A_0 of relativistic projectile residuals as a function of their excitation energy E_x/A according to the fireball model of Gosset *et al.* [43], calculated for ^{107}Sn projectiles, and INC calculations for ^{197}Au + C [44] (dashed lines), according to the experimental results for ^{197}Au nuclei reported by Pochodzalla *et al.* [27] and including the widths in E_x/A (dots) and according to the parametrization used in this work for $a_2 = 0.012$ and 0.015 MeV^{-2} (solid lines). Bottom panel: Ensemble of hot thermal sources represented in a scatter plot of reduced mass number A/A_0 versus excitation energy E_x/A, as used in the SMM calculations. The frequency of the individual sources is proportional to the area of the squares.

statistical descriptions [24,47,49,50]. A considerable part of the accumulated energy is not distributed statistically at freeze-out, as evident from the fragment kinetic energies, which are much higher than their thermal expectations [54].

In the present work, we follow the procedure used by Botvina *et al.* [14], which was rather effective in describing the multifragmentation of relativistic ^{197}Au projectiles, including their correlations and dispersions. There, the average masses of the equilibrated sources A_s were parametrized as $A_s/A_0 = 1 - a_1(E_x/A_s) - a_2(E_x/A_s)^2$, where E_x is the excitation energy of the sources in MeV and A_0 is the projectile mass. The correlations obtained with parameters $a_1 = 0.001$ MeV^{-1} and $a_2 = 0.015$ MeV^{-2}, used in Ref. [14], as well as $a_2 = 0.012$ MeV^{-2} are shown in Fig. 5. It is interesting to note that a nearly identical correlation was obtained by Désesquelles *et al.* [51] with a linear backtracing algorithm based on the SMM and on the fragmentation observables measured for ^{197}Au + Cu at 600 MeV/nucleon. As argued in Ref. [47], a dependence of this kind can be considered as consistent with BUU calculations.

The ensemble of thermal sources adopted for the present analysis, for $a_2 = 0.015$ MeV^{-2}, is given in the bottom panel of Fig. 5 as a weighted distribution in the A_s/A_0 versus E^*/A_s plane. The widths are empirically adjusted, guided by the earlier results for ^{197}Au fragmentation [14]. The yield distributions as functions of the reduced mass A/A_0 and excitation energy per nucleon were also generated empirically, in a similar manner as described in the same reference. Identical parameters were used for the three reaction systems. The charges of the sources were determined by assuming that the charge-to-mass ratio Z/A remains that of the initial projectiles. This is expected for the initial reaction phase, as long as nucleon-nucleon dynamics dominates, and supported by INC and relativistic BUU calculations for similar collision systems [36,39]. Further arguments in favor of this assumption derived from the experimental neutron-to-proton ratios of emitted fragments are discussed in Sec. VI.

C. Model description

As the model for multifragmentation, describing the reaction stages (2) and (3) defined above, the statistical multifragmentation model (SMM, for a review see Ref. [2]) is used. The SMM assumes statistical equilibrium of the excited nuclear system with mass number A_s, charge Z_s, and excitation energy E_x (above the ground state) within a low-density freeze-out volume. All breakup channels (partitions $\{p\}$) composed of nucleons and excited fragments are considered and the conservation of baryon number, electric charge, and energy are taken into account. Besides the breakup channels, also the compound-nucleus channels are included and the competition between all channels is permitted. In this way, the SMM covers the conventional evaporation and fission processes occurring at low excitation energy as well as the transition region between the low- and high-energy deexcitation regimes. In the thermodynamic limit, as demonstrated in Refs. [55–57], the SMM is consistent with the nuclear liquid-gas phase transition when the liquid phase is represented by an infinite nuclear cluster.

In the model, light nuclei with mass number $A \leqslant 4$ and charge $Z \leqslant 2$ are treated as elementary stable particles with masses and spins taken from the nuclear tables ("nuclear gas"). Only translational degrees of freedom of these particles contribute to the entropy of the system. Fragments with $A > 4$ are treated as heated nuclear liquid drops. Their individual free energies F_{AZ} are parametrized as a sum of the bulk, surface, Coulomb, and symmetry energy contributions:

$$F_{AZ} = F^B_{AZ} + F^S_{AZ} + E^C_{AZ} + E^{\rm sym}_{AZ}. \quad (1)$$

The standard expressions for these terms are $F^B_{AZ} = (-W_0 - T^2/\epsilon_0)A$, where T is the temperature, the parameter ϵ_0 is related to the level density, and $W_0 = 16$ MeV is the binding energy of infinite nuclear matter; $F^S_{AZ} = B_0 A^{2/3}[(T_c^2 - T^2)/(T_c^2 + T^2)]^{5/4}$, where $B_0 = 18$ MeV is the surface energy coefficient and $T_c = 18$ MeV is the critical temperature of infinite nuclear matter; $E^C_{AZ} = cZ^2/A^{1/3}$, where $c = (3/5)(e^2/r_0)[1 - (\rho/\rho_0)^{1/3}]$ is the Coulomb parameter (obtained in the Wigner-Seitz approximation) with the charge unit e and $r_0 = 1.17$ fm; and $E^{\rm sym}_{AZ} = \gamma(A - 2Z)^2/A$, where $\gamma = 25$ MeV is the symmetry energy parameter. These parameters are those of the Bethe-Weizsäcker formula and correspond to the assumption of isolated fragments with normal density in the freeze-out configuration, an assumption found to be quite successful in many applications.

Within the microcanonical treatment [2,58] the statistical weight of a partition p is calculated as

$$W_p \propto \exp S_p, \quad (2)$$

where S_p is the corresponding entropy, depending on the fragments in this partition as well as on the parameters of the system. In the grand canonical treatment of the SMM [59], after integrating out translational degrees of freedom, the mean multiplicity of nuclear fragments with A and Z can be written as

$$\langle N_{AZ}\rangle = g_{AZ}\frac{V_f}{\lambda_T^3}A^{3/2}\exp\left[-\frac{1}{T}(F_{AZ} - \mu A - \nu Z)\right]. \quad (3)$$

Here g_{AZ} is the ground-state degeneracy factor of species (A, Z), $\lambda_T = (2\pi\hbar^2/m_N T)^{1/2}$ is the nucleon thermal wavelength, and $m_N \approx 939$ MeV/c^2 is the average nucleon mass. V_f is the free volume available for the translational motion of fragments. The free energy $F_{AZ} = F_{AZ}(T, \rho)$ of fragments with $A > 4$ and $Z > 2$, parametrized as given above, is a function of the temperature and density. The chemical potentials μ and ν are found from the mass and charge constraints:

$$\sum_{(A,Z)}\langle N_{AZ}\rangle A = A_s, \quad \sum_{(A,Z)}\langle N_{AZ}\rangle Z = Z_s. \quad (4)$$

For the freeze-out density, one-third the normal nuclear density is assumed. This is a standard value, used previously in many successful applications and consistent with independent experimental determinations of the freeze-out density [60,61].

For generating individual multifragmentation events, the methods proposed in Refs. [2,14] have been used. Individual sources are randomly selected from the ensemble of excited sources according to their probability of occurrence within the ensemble (Fig. 5) up to a total of typically 10^5 to 10^6 sources.

Their breakup is calculated with the SMM by the Monte-Carlo method described in Ref. [2], which has the advantage of a high efficiency. In particular, at low excitation energies, when partitions of primary hot fragments with small total multiplicities M dominate, the probabilities of all partitions with $M \leqslant 3$, including the compound nucleus formation, are included.

As a first step, partitions are randomly selected from the ensemble of all possible partitions and their probabilities are determined. For small fragment multiplicities, the microcanonical sampling according to Eq. (2) can be performed. At higher excitation energy, typically above $E_x \approx 4$ MeV/nucleon, the masses and charges of primary hot fragments are generated according to the grand-canonical distribution (Eq. [4]), however, by requiring the exact mass number and charge conservations in each partition. The temperature of a partition is found iteratively by adjusting it so that the total energy is conserved. It is, therefore, referred to as the microcanonical temperature of the partition. After their formation in the freeze-out volume, the fragments propagate independently in their mutual Coulomb fields and undergo secondary decays. The deexcitation of the hot primary fragments proceeds via evaporation, fission, or via Fermi breakup for primary fragments with $A \leqslant 16$ [62].

Because the calculated events contain all particles and fragments with their masses, charges, and momenta including those produced in secondary decays, they can be treated in the same way as experimental events. Sorting into event groups can be performed and group averages and distributions or correlations can be determined. Before comparisons with experimental data are made, the resulting partitions of cold fragments are subjected to the ALADIN experimental filter by randomly removing fragments according to the Z-dependent acceptance given in Sec. II.

D. In-medium modification of fragment properties

The liquid-drop model for the description of the emerging fragments is an essential and very successful ingredient of the SMM [2]. It is based on the concept of an idealized chemical freeze-out, defined as the moment in time at which the nuclear forces have ceased to act between fragments. Their action within fragments can then be summarized with a liquid-drop description of the fragment properties with standard parameters. Only the Coulomb energy is reduced due to the presence of other fragments, an effect reasonably well accounted for within the Wigner-Seitz approximation [2]. However, in a more realistic treatment of the breakup stage, the excited primary fragments may have to be considered as not only excited but also having modified properties due to residual interactions with the environment. Their shapes and average densities may deviate from the equilibrium properties of isolated nuclei [63,64]. Evidence for such effects has already been obtained from dynamical simulations [65] and from dynamical or statistical analyses of isotopic effects in a variety of reactions [22,36,66,67]. Within the statistical approach, they can be accounted for in the fragment free energies by changing the corresponding liquid-drop parameters. In the following, we search for such effects by testing the sensitivity of fragment observables to the surface and symmetry energy terms in comparison with the present data.

At the last stage of the multifragmentation process, the hot primary fragments undergo deexcitation and propagate in the mutual Coulomb field. The realistic description of this stage is essential for obtaining reliable final fragment yields. To the extent that this can be achieved, the hot breakup stage will become accessible, which is the preeminent aim of this work. Possible modifications of the fragment properties must be taken into account in the first deexcitation steps, as the hot fragments are still surrounded by other species, while, at the end of the evaporation cascade, the standard properties must be restored. In the actual calculations, a linear interpolation between these two limiting cases has been introduced in the interval of excitation energies between zero and $E_x^{\mathrm{int}} = 1$ MeV/nucleon [68]. Energy and momentum conservation are observed throughout this process.

Possible in-medium modifications of light clusters with $A \leqslant 4$, treated as elementary particles in the SMM, are not considered here. This seems justified because of their small primary multiplicities in the multifragmentation channels. For example, in the primary partitions of a single source ^{124}Sn at $E_x = 5$ MeV/nucleon, ^{2,3}H and ^{3,4}He nuclei appear with mean multiplicities of 0.14, 0.07, 0.03, and 0.29, respectively. Together they amount to a fraction of less than 1.5% of the total mass of the system. The majority of light clusters observed in the final partitions stem from secondary decays [69]. Modifications of light clusters have been intensively studied with microscopic approaches, preferentially however in temperature-density domains at which larger fragments are of reduced importance (see, e.g., Refs. [70,71] and references given therein).

IV. CHARGE CHARACTERISTICS OF FRAGMENT PARTITIONS

A. Ensemble normalization

For event characterization, the total charge bound in fragments with $Z \geqslant 2$, Z_{bound}, has been introduced as in previous reports on ALADIN results (see, e.g., Refs. [12,14,23,24]). Small Z_{bound} values correspond to high excitation energies of the sources that disintegrate predominantly into very light clusters ("fall" of multifragmentation). Large values of Z_{bound} correspond to low excitation energies, at which the decay changes its character from evaporationlike/fissionlike processes to multifragmentation ("rise" of multifragmentation).

In Fig. 4, besides the experimental also the theoretical event distributions as a function of Z_{bound} are shown for the three projectiles under investigation, ^{107}Sn, ^{124}Sn, and ^{124}La. The theoretical results are obtained with the ensembles introduced in the previous section (Fig. 5) and with standard assumptions regarding the fragment properties, i.e., $B_0 = 18$ MeV and $\gamma = 25$ MeV for the surface- and symmetry-term coefficients. As Z_{bound} is approximately equal to the charge of the spectator system and only slightly affected by its excitation energy, the comparison is mainly a test of how well the ensemble parameters are chosen. Modifications of

the liquid-drop parameters have a very small effect on the $Z_{\rm bound}$ spectra.

The agreement between theory and experiment is overall very satisfactory and sufficient for performing the following analyses in individual intervals of $Z_{\rm bound}$. A larger disagreement is observed in the region of $Z_{\rm bound} > 40$ for the Sn projectiles and at $Z_{\rm bound} > 46$ for the ^{124}La projectile (Fig. 4). As discussed above, it may be partly of experimental origin. The discrepancies at very small $Z_{\rm bound} < 10$ are mainly occurring in channels dominated by multi-α events. Here, the larger experimental yields may come from more central collisions that are beyond the statistical treatment of the spectator multifragmentation studied here. For these reasons, the following analysis mainly focuses on the intermediate range of $Z_{\rm bound} \approx 10$–40 (46 in the case of ^{124}La), constituting the major part of the rise and fall of nuclear multifragmentation.

For the quantitative comparison of theory and experiment, the SMM ensemble calculations were globally normalized with respect to the measured $Z_{\rm bound}$ cross sections in the interval $10 < Z_{\rm bound} \leqslant 30$ for which the agreement is best. The obtained factors are 0.009 37 mb, 0.008 04 mb, and 0.0106 mb per theoretical event for ^{107}Sn, ^{124}Sn, and ^{124}La projectiles, respectively, i.e., on average about 100 events per mb were calculated with the SMM.

B. Sensitivity to liquid-drop parameters

As a first step, the sensitivity of the fragment-charge distributions and correlations to the intrinsic properties of these fragments was investigated with the SMM. Ensemble calculations were performed for different parameters of the liquid-drop description of the produced fragments and analyzed as a function of the obtained $Z_{\rm bound}$. To permit a more detailed comparison and to include the case of ^{124}La on the same scale, the reduced $Z_{\rm bound}/Z_0$, normalized with respect to the atomic number Z_0 of the projectile, has been used for some observables and subdivided into five bins (0–0.2, 0.2–0.4, etc.), labeled by their central values (0.1, 0.3, etc.) in the legends of the figures.

For the case of ^{124}Sn, the relative fragment yields as a function of Z sorted into these five bins are shown in Fig. 6. The charge distribution evolves from a so-called "U-shaped" distribution, with domination of evaporation of the compound nucleus and asymmetric binary decay during the onset of multifragmentation, to a rapidly dropping exponential distribution. This evolution is a characteristic feature of the present type of spectator fragmentation [23,25,72]. The variation of the symmetry-term coefficient in the calculations, down to one-third of its standard value, has a negligible effect on the resulting charge distributions except in the bin of largest $Z_{\rm bound}$. There the fragment yields in the intermediate-mass range, which are already small, are further reduced if smaller γ parameters are chosen.

The same conclusion can be drawn from the results for the multiplicities of intermediate-mass fragments (IMF, $3 \leqslant Z \leqslant 20$) shown in Fig. 7 as functions of $Z_{\rm bound}$ for the neutron-rich ^{124}Sn and the neutron-poor ^{124}La projectiles. The effect of varying the symmetry-term coefficient is very small and visible only at the rise of multifragmentation in the right half of the

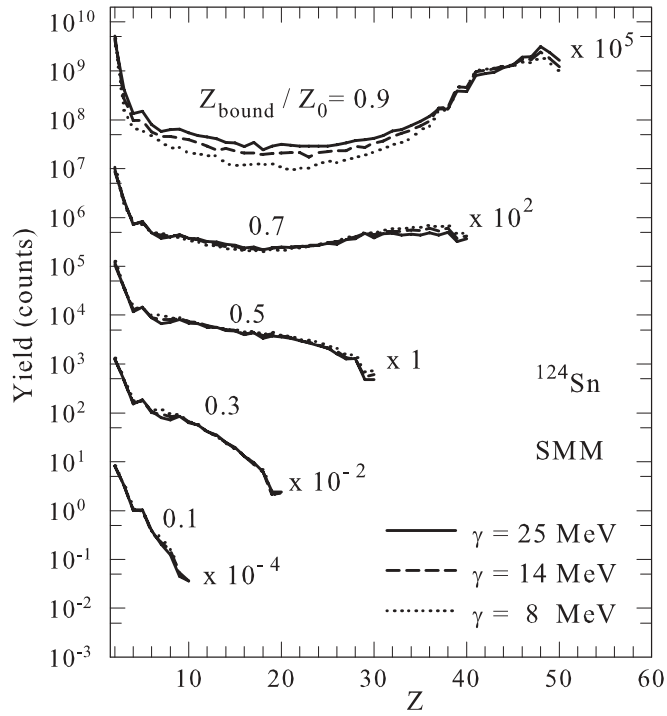

FIG. 6. Relative yields of fragments for 10-unit-wide intervals of $Z_{\rm bound}$ as obtained with the SMM for the standard symmetry-term coefficient $\gamma = 25$ MeV (solid lines) and with reduced coefficients $\gamma = 14$ and 8 MeV (dashed and dotted lines, respectively) as a function of the fragment Z for the case of ^{124}Sn projectiles. The centers of the five $Z_{\rm bound}$ intervals relative to Z_0 and the scale factors used for displaying the yields are indicated in the figure.

figure. The fall part is expected to be universal because of the autocorrelation of the two quantities $M_{\rm imf}$ and $Z_{\rm bound}$ [73]. The autocorrelations dominate in the cases of $Z_{\rm bound} = 3$ and 5, which can only be reached with partitions containing exactly one lithium fragment.

The surface energy of fragments is important for the charge yields [74]. As demonstrated in Figs. 8 and 9, the relatively small variation of the surface-energy coefficient B_0 from 18 to 20 MeV leads to considerable changes in the fragment production. The larger surface energy suppresses multifragmentation, leading to smaller IMF yields and multiplicities. And, vice versa, decreasing B_0 results in an intensive breakup of nuclei already at low excitation energy and to steeper Z spectra. Because of the mentioned autocorrelations, the influence of B_0 decreases with decreasing $Z_{\rm bound}$, as evident from both figures.

C. Data comparison

The measured cross sections $d\sigma/dZ$ for fragment production in reactions initiated by ^{107}Sn, ^{124}Sn, and ^{124}La projectiles are shown in Figs. 10–12. The data have been sorted into five bins of the reduced bound charge $Z_{\rm bound}/Z_0$ of width 0.2 spanning the range up to $Z_{\rm bound} = Z_0$. The evolution from U-shaped to exponential Z spectra, already discussed in the previous section, appears without noticeable differences between the three cases.

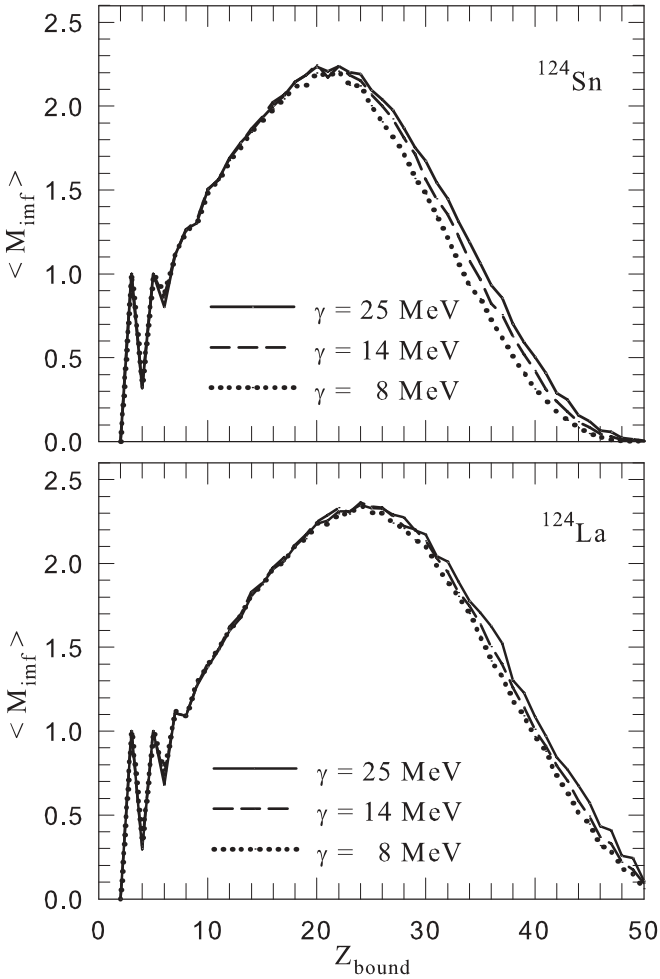

FIG. 7. Mean multiplicity of intermediate-mass fragments, $\langle M_{\rm imf}\rangle$, as a function of $Z_{\rm bound}$ as obtained with the SMM for the standard symmetry-term coefficient $\gamma = 25$ MeV (solid lines) and with reduced coefficients $\gamma = 14$ and 8 MeV (dashed and dotted lines, respectively), for reactions of ^{124}Sn (top) and ^{124}La (bottom) projectiles.

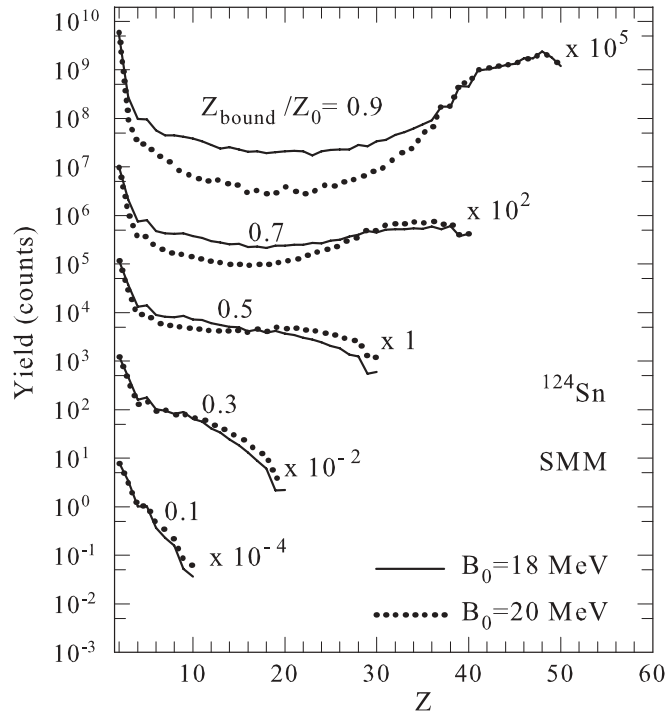

FIG. 8. Relative yields of fragments for 10-unit-wide intervals of $Z_{\rm bound}$ as obtained with the SMM for the standard surface-term coefficient $B_0 = 18$ MeV (solid lines) and with the modified coefficient $B_0 = 20$ MeV (dotted line) as a function of the fragment Z for the case of ^{124}Sn projectiles. The centers of the five $Z_{\rm bound}$ intervals and the scale factors used for displaying the relative yields are indicated in the figure.

The results of the SMM calculations, represented by the thin lines in the figures, were obtained with the normalized ensembles (parameter $a_2 = 0.015$ MeV^{-2}, cf. Fig. 5) and with liquid-drop parameters that provide an adequate description of the experimental observables and trends. The charge observables are mostly sensitive to the surface-term coefficient B_0, as discussed in the previous section. In order to maintain a consistent comparison, the evidence for a reduced symmetry-term coefficient γ in the fragmentation channels, extracted from the analysis of isotope characteristics in Sec. V, has already been taken into account by choosing $\gamma = 14$ MeV for the three systems.

For the surface-term coefficient, different values had to be chosen in order to obtain equivalent descriptions for the neutron-rich and neutron-poor systems. The good reproduction of the charge distributions (Figs. 10–12) and of the charge correlations shown in Figs. 13 and 14 has been achieved with the values $B_0 = 17.5$ MeV for ^{124}Sn and $B_0 = 19.0$ MeV for the neutron-poor ^{107}Sn and ^{124}La. They are determined with an accuracy of about 0.5 MeV for the chosen ensemble of excited sources (cf. Figs. 8 and 9). It should be mentioned here again that the comparisons are made with the measured data and that the small inefficiencies of the spectrometer for very light fragments are taken into account by filtering the calculations. If corresponding corrections are applied to the data, as done in Ref. [35], the main effect is a shift of the maxima of the mean fragment multiplicity to about 10% larger values of $Z_{\rm bound}$ than shown in Fig. 14, while the increase in the maximum multiplicity itself is nearly negligible.

If modifications of the source parameters are simultaneously permitted, the effect of B_0 on fragment multiplicities can be compensated by a corresponding variation of a_2. The larger mean multiplicities $\langle M_{\rm imf}\rangle$ and the shift of the peak of the multiplicity distribution to larger $Z_{\rm bound}$ observed by reducing the surface term (Fig. 9) can also be obtained by increasing the excitation energies of the sources [74]. Equally satisfactory results for ^{124}Sn were, e.g., obtained with the parameter pair $a_2 = 0.015$ MeV^{-2} and $B_0 = 17.5$ MeV used here as well as with $a_2 = 0.012$ MeV^{-2} and $B_0 = 19.0$ MeV. The required N/Z dependence of B_0 is independent of this ambiguity, at least as long as the ensemble parameters remain the same and independent of the projectile N/Z.

Evidence for a variation of the surface-term coefficient with the isotopic composition of the system has previously been derived from a τ analysis of fragment-charge yields $y(Z)$

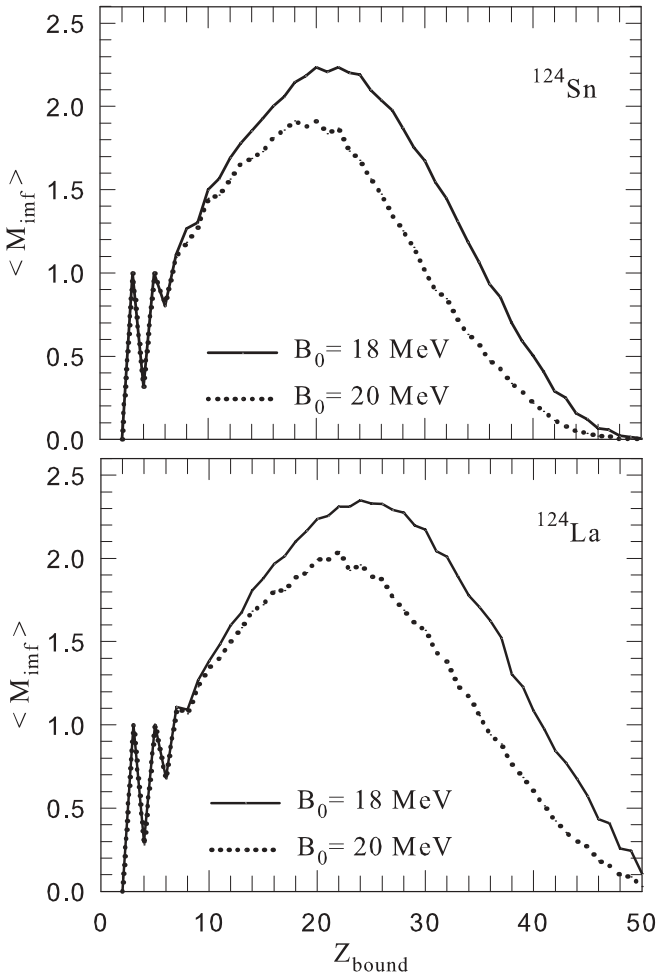

FIG. 9. Mean multiplicity of intermediate-mass fragments, $\langle M_{\rm imf}\rangle$, as a function of $Z_{\rm bound}$ obtained with the SMM for the standard surface-term coefficient $B_0 = 18$ MeV (solid lines) and with the modified coefficient $B_0 = 20$ MeV (dotted lines), for reactions of ^{124}Sn (top) and ^{124}La (bottom) projectiles.

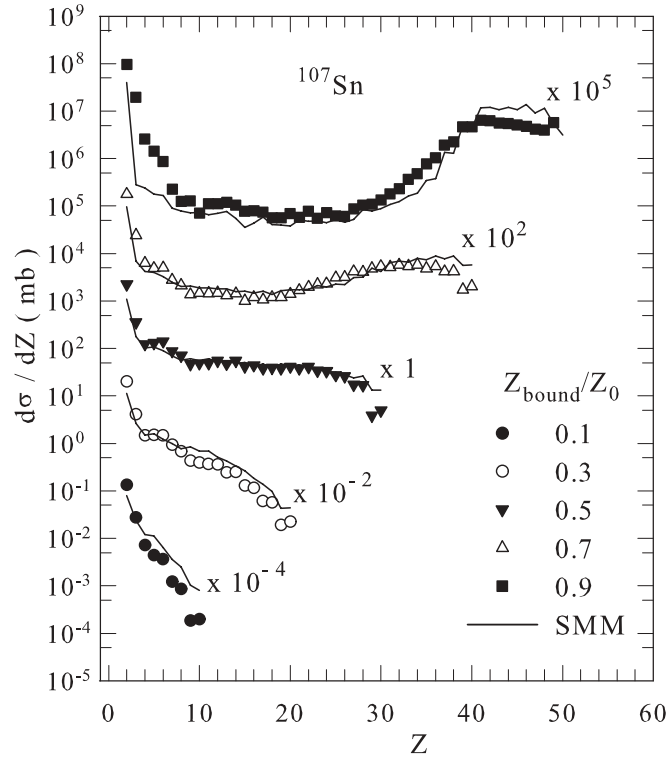

FIG. 10. Experimental cross sections $d\sigma/dZ$ for the fragment production following collisions of ^{107}Sn projectiles sorted into five intervals of $Z_{\rm bound}/Z_0$ with centers as indicated and width 0.2 (symbols) in comparison with normalized SMM calculations (lines). Different scale factors were used for displaying the cross sections as indicated.

measured for the fragmentation of ^{129}Xe, ^{197}Au, and ^{238}U at 600 MeV/nucleon [74]. Near the onset of multifragmentation ($Z_{\rm bound}/Z_0 > 0.6$), the τ parameters obtained from power-law fits according to $y(Z) \propto Z^{-\tau}$ in the range $5 \leqslant Z \leqslant 15$ are larger for the projectiles with smaller N/Z while the opposite is predicted by the SMM for constant B_0. There, the variation of the N/Z of the studied systems was accompanied by a considerable change in mass. The present data confirm that the observed inversion of the hierarchy of τ with respect to the predictions with constant B_0 is indeed an isotopic effect. The τ parameters are larger for the two neutron-poor systems at large $Z_{\rm bound}/Z_0$ (Fig. 15). For the further conclusion that the N/Z dependence of B_0 may disappear at higher excitations [74] no additional evidence is obtained from the present data. In fact, the sensitivity of the Z spectra to B_0 is seen to diminish at smaller $Z_{\rm bound}$ (Fig. 8) and the fragment multiplicities as a function of $Z_{\rm bound}$ become universal (Fig. 9).

A variation of the surface term with N/Z is similar to a surface dependence of the symmetry energy, i.e., an additional term $\gamma_s \cdot A^{2/3}(A-2Z)^2/A^2$ in the liquid-drop parametrization. Using the effective A/Z values of the two secondary beams and $\Delta B_0 = 1.5$ MeV and averaging over the two pairs of systems, ^{124}Sn vs ^{107}Sn and ^{124}Sn vs ^{124}La, yields a coefficient $\gamma_s = 45$ MeV. This is larger than parameters of standard mass formulas. That of Myers and Swiatecki [75], e.g., contains 28.1 and 33.2 MeV for the volume and surface coefficients of the symmetry term, respectively. The accuracy of the deduced N/Z dependence of B_0 is not sufficient to draw firm conclusions at this point. However, large surface effects are consistent with the results for the symmetry term derived from the fragment mass yields discussed in the following section.

Concluding the analysis of charge observables, it may be stated that an excellent overall description of the measured yields and correlations is obtained within the statistical approach. With the chosen ensemble of excited spectator nuclei and after a global normalization, the fragment yields and spectra shapes are reproduced on an absolute level (Figs. 10–12) and the correlations agree well with the data (Figs. 13 and 14). Deviations occur for very large $Z_{\rm bound}$ for which the yields of heavy fragments are overpredicted and those of light fragments ($Z < 10$) are underpredicted. They should not be overrated, however, because the incomplete trigger efficiency in the experiment (Sec. II) and the empirical character of the yield function of the theoretical source ensem-

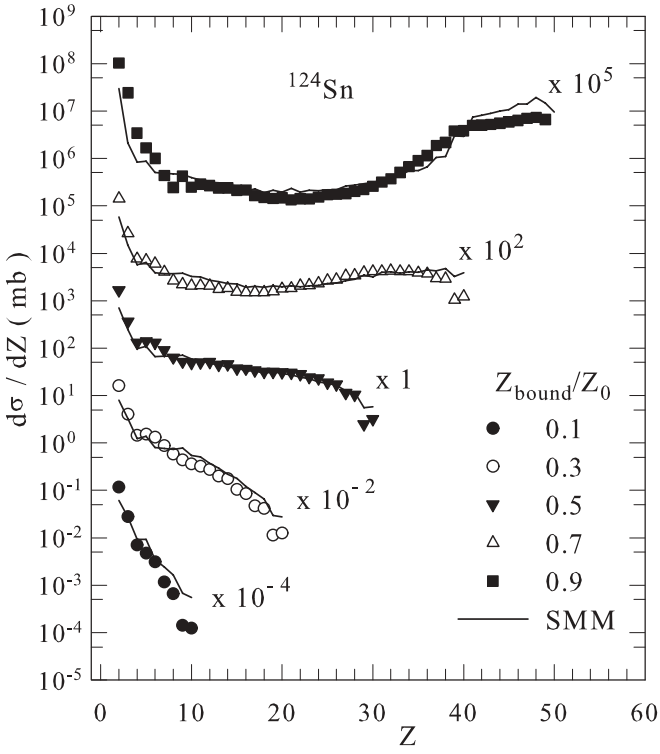

FIG. 11. As Fig. 10 but for the case of ^{124}Sn projectiles.

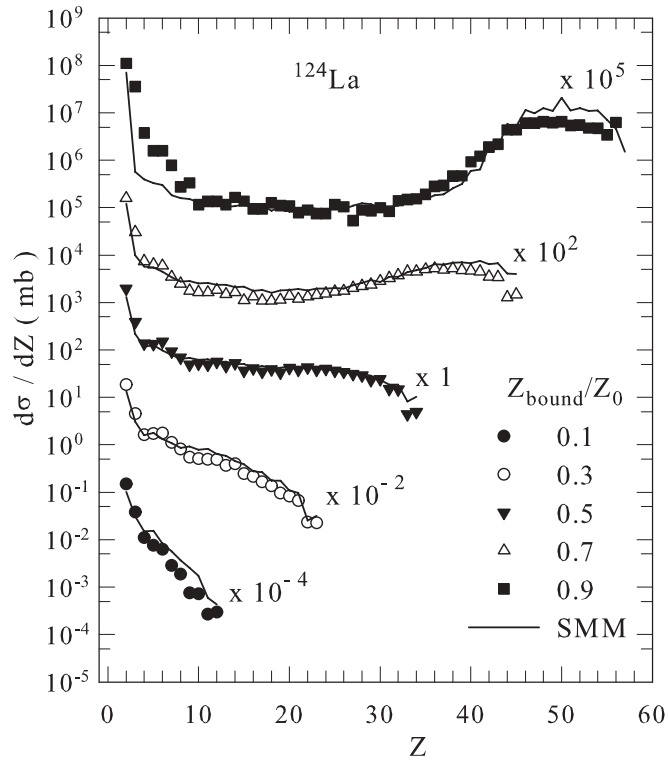

FIG. 12. As Fig. 10 but for the case of ^{124}La projectiles.

bles may both be causing them. In fact, the finite values for the fragment multiplicity for Z_{bound} approaching 50 in the tin cases seem to indicate a trigger bias favoring the more violent collisions.

V. ISOTOPE CHARACTERISTICS OF PRODUCED FRAGMENTS

A. Parameter dependence

The successful description of charge observables provides the basis for the investigation of the isotope distributions and the information contained therein. As in the previous section, the parameter dependence is studied first. For this purpose, the mean neutron-to-proton ratios $\langle N\rangle/Z$ are chosen. SMM calculations of this quantity for the two projectiles ^{124}Sn and ^{124}La and for different surface-term coefficients B_0 and different symmetry-term coefficients γ are presented in Figs. 16 and 17, respectively.

As evident from the figures, the situation is complementary to that encountered in the study of the charge observables as noted previously [76]. The surface parameter B_0 has practically no influence on the isotope distributions while the symmetry energy strongly affects the mean neutron richness of fragments, most noticeably for $Z \geqslant 7$. It increases with decreasing γ because of the correspondingly larger widths of the isotope distributions at freeze-out. At $Z \leqslant 6$, the mean neutron-to-proton ratios exhibit the known odd-even effects, typical for this type of reaction [77] and shown to result from secondary decays when the strongly bound even-even $N = Z$ nuclei attract a large fraction of the product yields [78,79].

The mean neutron numbers are larger for the fragments of ^{124}Sn by about half a mass unit, and the difference is larger if γ is reduced (Fig. 17). This difference, however, is much smaller than that of the primary fragments, which have nearly the same $\langle N\rangle/Z$ ratio as the primary thermal sources [58]. During the secondary deexcitation, the neutron richness of fragments will decrease as neutron emission dominates. In the case of small γ, this trend is reduced because the mass distribution of accessible daughter nuclei is wider and emissions of charged particles may more easily compete [68].

B. Isotope distributions

Cross sections measured for resolved isotopes and integrated over $0.2 \leqslant Z_{bound}/Z_0 \leqslant 0.8$ are presented in Figs. 18 and 19 for $Z = 3$–6 and $Z = 7$–10, respectively. The major part of the rise and fall of multifragmentation is covered by the selected Z_{bound} interval (Fig. 14). Because of the stringent sorting conditions required for producing background-free mass spectra, the experimental cross sections for isotope production were obtained by normalizing the mass-integrated fragment yields for a given Z with respect to the measured elemental cross section in the same Z_{bound} interval (Sec. II). The differences of the isotope distributions between the neutron-poor and neutron-rich cases are small but still visible in the logarithmic representation. In particular, the fragment yields on the neutron-rich side are considerably larger in the case of ^{124}Sn.

The SMM calculations shown in the figures were performed with the ensemble parameter $a_2 = 0.015$ MeV^{-2}, with

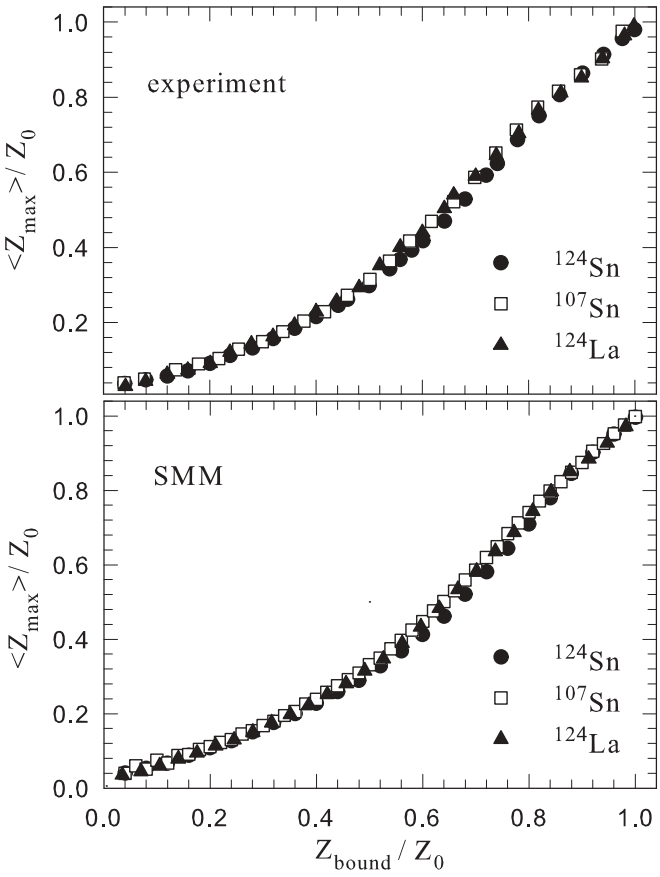

FIG. 13. Experimental results (top panel) and results of SMM calculations (bottom panel) for the mean maximum charge $\langle Z_{max}\rangle$ within an event versus Z_{bound}, both normalized with respect to Z_0, for the three studied projectiles.

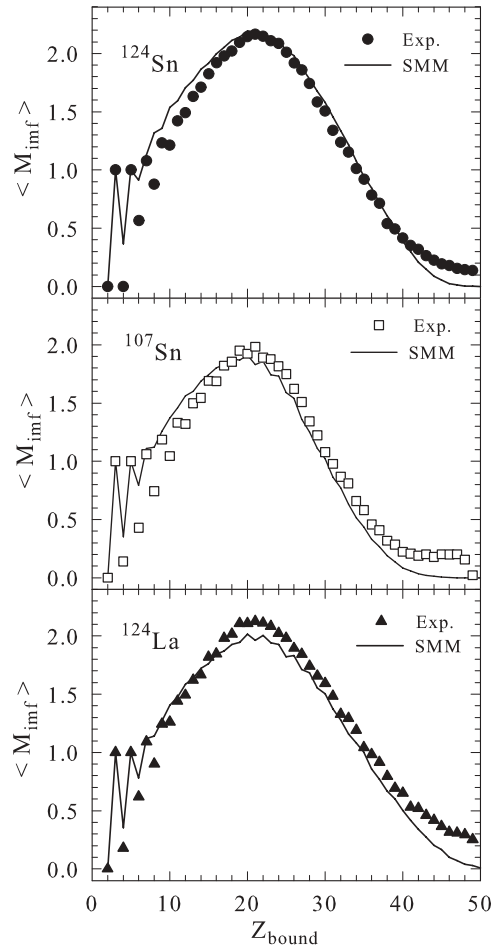

FIG. 14. Comparison of SMM calculations (lines) with the experimental results (symbols) for the mean multiplicity $\langle M_{imf}\rangle$ of intermediate-mass fragments versus Z_{bound} for the three studied projectiles.

$B_0 = 17.5$ and 19 MeV for the neutron-rich and neutron-poor projectiles, respectively, and for two choices of γ. For the standard calculations, the symmetry-term coefficient $\gamma = 25$ MeV was used for the hot fragments at breakup and throughout the secondary deexcitation stage. Modified calculations were performed with $\gamma = 14$ MeV and with the interpolation procedure for the secondary deexcitation at $E_x \leqslant 1$ MeV/nucleon (Sec. III). The calculated cross sections are globally normalized for each projectile case as described in Sec. IV A.

The comparison with the data shows that the yields of neutron-rich isotopes are much better described if the reduced symmetry-energy coefficient is used. In particular, the heavier fragments with $Z \geqslant 7$ are rather sensitive to the variation of γ, as already evident from Fig. 17. The same conclusion can be drawn from the comparison of the mean neutron-to-proton ratios $\langle N\rangle/Z$ for elements of $Z \leqslant 10$ with the experimental results (Fig. 20). Evidently, they depend very little on Z_{bound}, and the calculations are, therefore, only shown for the full range $0.2 \leqslant Z_{bound}/Z_0 < 0.8$. The modified calculations, with $\gamma = 14$ MeV, agree well with the data, both with regard to the average magnitude as well as to the odd-even structures as a function of Z. The latter, however, are slightly more pronounced in the calculations than in the experiment for $Z \leqslant 6$ while the opposite is the case for larger fragments. This small difference may be connected to the discontinuity caused by the mass limit $A \leqslant 16$ set for using the Fermi breakup in the secondary-decay part of the calculations.

The ambiguity in the choice of the ensemble and surface-term parameters a_2 and B_0 discussed in Sec. IV C does not affect this result. In Fig. 21, calculations are shown that were performed with several combinations of these parameters, all capable of reproducing the charge observables. The observed mean $\langle N\rangle/Z$ is only reached with the reduced symmetry-term coefficient $\gamma = 14$ MeV.

Another important parameter is related to the secondary-deexcitation stage of the calculations. For the restoration of the standard symmetry-term coefficient, a linear interpolation between the initially reduced value and $\gamma = 25$ MeV of isolated nuclei in the interval of excitation energies below $E_x^{int} = 1$ MeV/nucleon has been adopted (end of Sec. III). The evaporation times corresponding to this energy are of the order of 10^{-21} s, which seems long, and one may argue that the restoration should start at a higher initial value E_x^{int}, possibly closer to 3 MeV/nucleon, which would correspond to a thermal freeze-out at $T \approx 5$ MeV [34]. Ensemble calculations performed with this choice for the ^{124}Sn and ^{124}La systems

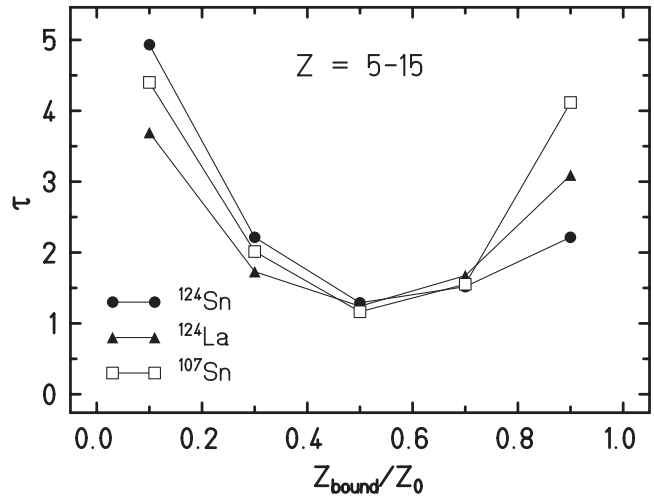

FIG. 15. Parameter τ obtained from power-law fits to the fragment yields $y(Z)$ in the range $5 \leqslant Z \leqslant 15$ according to $y(Z) \propto Z^{-\tau}$ as a function of Z_{bound}/Z_0.

also provide an excellent description of the data (Fig. 22). It is even superior in the range $Z \geqslant 6$ where the odd-even staggering of $\langle N \rangle / Z$ is much better reproduced than with $E_x^{\text{int}} = 1$ MeV//nucleon (cf. Fig. 20). It requires, however, an even larger reduction of the symmetry term coefficient γ to values below 10 MeV. Therefore, to the extent that $E_x^{\text{int}} = 1$ MeV/nucleon has to be considered as a lower limit for the beginning restoration of the properties of isolated nuclei,

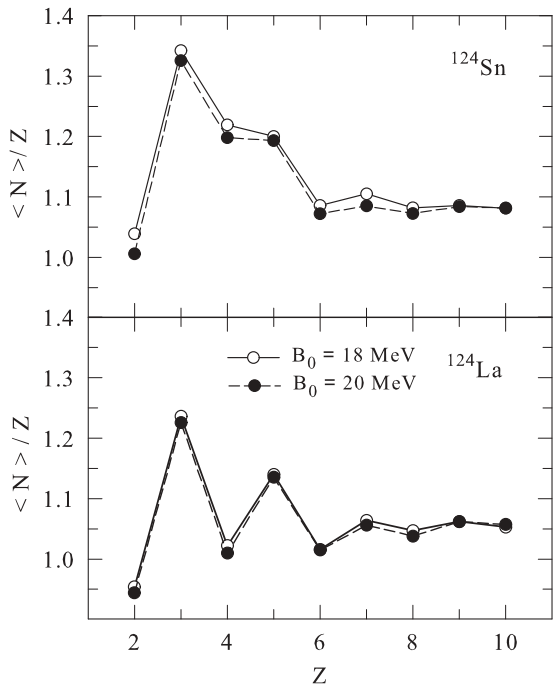

FIG. 16. SMM calculations of the mean neutron-to-proton ratio $\langle N \rangle / Z$ of fragments with $2 \leqslant Z \leqslant 10$ produced in the fragmentation of ^{124}Sn (top panel) and ^{124}La (bottom panel) projectiles for the interval $0.4 \leqslant Z_{\text{bound}}/Z_0 < 0.6$ as a function of the fragment Z, performed with $\gamma = 25$ MeV and with two surface energy coefficients $B_0 = 18$ and 20 MeV.

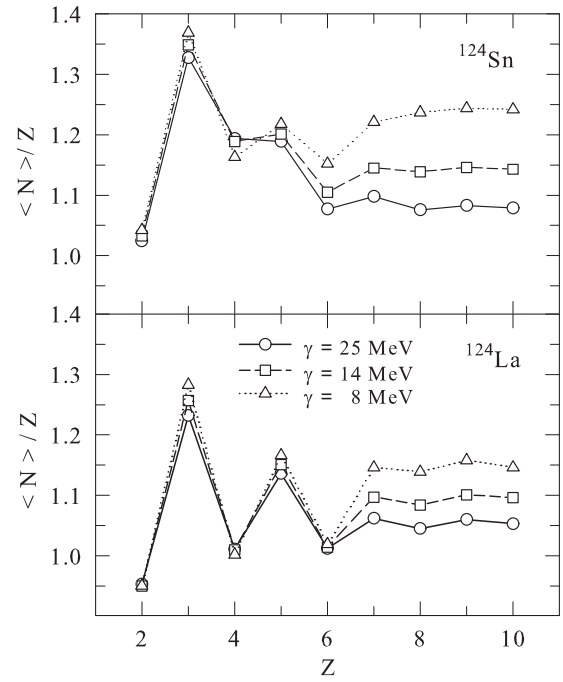

FIG. 17. SMM calculations of the mean neutron-to-proton ratio $\langle N \rangle / Z$ as in Fig. 16, but for $B_0 = 18$ MeV and three different symmetry energy coefficients $\gamma = 8$, 14, and 25 MeV.

the reduced $\gamma = 14$ MeV represents an upper limit for the symmetry-term coefficient needed to reproduce the observed neutron richness of intermediate-mass fragments.

Summarizing this section it may be stated that the isotopically resolved fragment yields provide evidence for a reduced symmetry energy in the hot environment at freeze-out, in accordance with previous findings [22,36]. Similar observations were made in reaction studies performed at intermediate and relativistic energies [66,67,76,80,81].

VI. DISCUSSION OF FREEZE-OUT PROPERTIES

A. Source properties

Several reasonable but also essential assumptions have been made in the statistical analysis presented so far. In particular, for the N/Z ratios of the considered ensembles those of the initial projectiles have been used. At relativistic energies, the preequilibrium particles are mainly produced in individual nucleon-nucleon collisions and, on average, the neutron-to-proton ratios should not change. This is contrary to the situation in the intermediate-energy range (beam energies less than 100 MeV/nucleon) where a considerable isospin diffusion has been identified [82]. Studying this in more detail with INC or BUU calculations shows that, at relativistic energies, a slight decrease of the neutron richness with increasing excitation energy has to be expected. It is not strongly dependent on the initial N/Z so that the difference between the isotopic compositions of different residue systems does not change by more than a few percent during the initial reaction stages [36,39]. This result is essential for the conclusions drawn from the isoscaling study of Le Fèvre *et al.* [36] as well

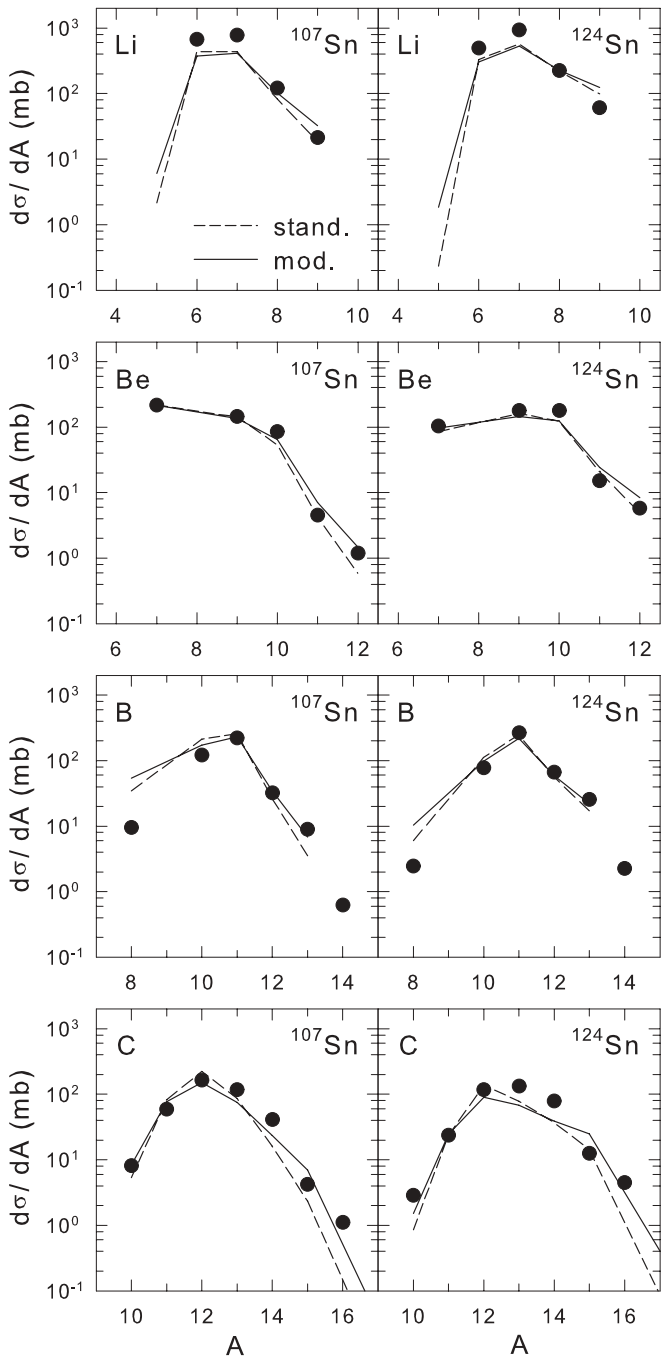

FIG. 18. Isotope distributions of fragments with $Z = 3$–6 for ^{107}Sn (left panels) and ^{124}Sn (right panels), integrated over $0.2 \leqslant Z_{\rm bound}/Z_0 \leqslant 0.8$. The dots represent the experimental data. Normalized results from calculations with the standard and modified parameters are shown by the dashed and solid lines, respectively.

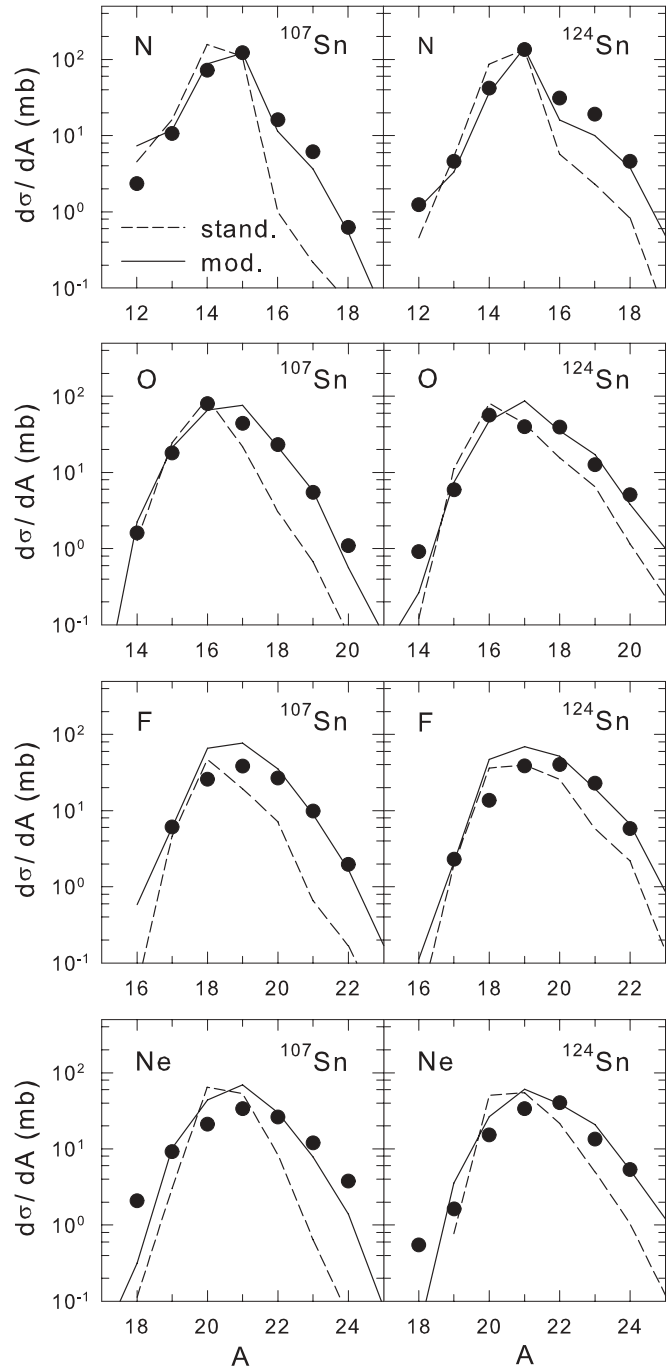

FIG. 19. Isotope distributions for ^{107}Sn (left panels) and ^{124}Sn (right panels) as in Fig. 18 but for fragments with $Z = 7$–10.

as for the isoscaling analysis presented further below. The isoscaling parameter α is roughly proportional to the difference of the N/Z ratios of the studied systems so that a reduction of the latter, before the chemical fragment composition is established, would naturally explain the observed decrease of α.

The situation is different for the analysis of the $\langle N\rangle/Z$ ratios of light fragments presented in the previous section, as illustrated in Fig. 23. Two calculations were performed for ^{124}Sn ensembles, one with the original $N/Z = 1.48$ of this projectile and one with a considerably smaller neutron-to-proton ratio $N/Z = 1.33$, which is halfway between those of the ^{124}Sn and of the neutron-poor ^{124}La and ^{107}Sn nuclei. As expected, the $\langle N\rangle/Z$ ratios of the produced fragments are lower for the smaller initial N/Z than for the original choice. To raise them to the experimental level an even larger reduction of the γ parameter would be necessary. A larger than assumed variation of the isotopic composition of the thermal

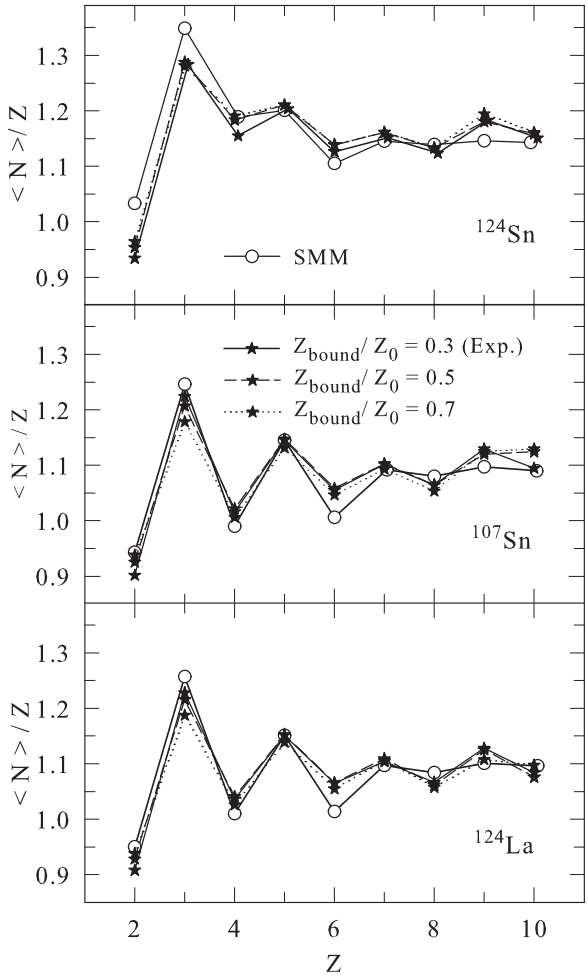

FIG. 20. Measured mean neutron-to-proton ratios $\langle N\rangle/Z$ for fragments with $Z \leqslant 10$ produced in the multifragmentation of ^{124}Sn (top panel), ^{107}Sn (middle panel), and ^{124}La projectiles (bottom panel) and for three intervals of Z_{bound}/Z_0 with centers as indicated and widths 0.2 (stars). In the calculations, performed for the range $0.2 \leqslant Z_{\text{bound}}/Z_0 < 0.8$, the surface-energy coefficients $B_0 = 18$ MeV and the symmetry-energy coefficient $\gamma = 14$ MeV were used (open circles).

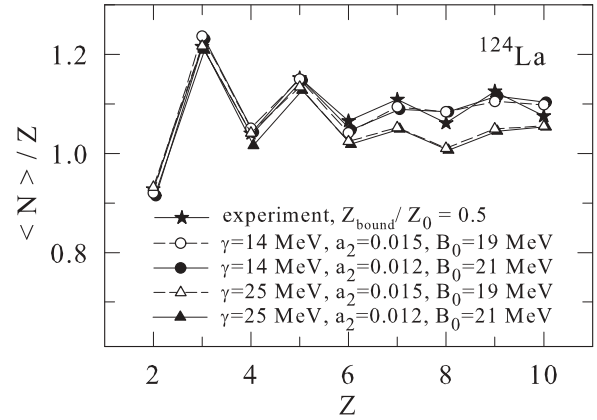

FIG. 21. Mean neutron-to-proton ratio $\langle N\rangle/Z$ of fragments with $Z \leqslant 10$ produced in the fragmentation of ^{124}La projectiles in the range $0.4 \leqslant Z_{\text{bound}}/Z_0 < 0.6$. The experimental results (stars) are compared with SMM calculations using four combinations of symmetry-energy, ensemble, and surface parameters as indicated. Only the calculations with the symmetry-energy coefficient $\gamma =$ 14 MeV (circles) are close to the data.

sources at breakup will thus not affect the previously reached conclusion.

B. Freeze-out temperature

Chemical freeze-out temperatures, as obtained from double-isotope-yield ratios measured in this experiment, have been presented and discussed in Ref. [35]. The two observables shown in Fig. 24 as a function of the normalized Z_{bound} are the frequently used

$$T_{\text{HeLi}} = 13.3\text{MeV}/\ln\left(2.2\frac{Y_{^6\text{Li}}/Y_{^7\text{Li}}}{Y_{^3\text{He}}/Y_{^4\text{He}}}\right), \quad (5)$$

based on the ^{3}He/^{4}He and ^{6}Li/^{7}Li yield ratios, where Y denotes the isotopically resolved yields (left panel, Ref. [27]), and

$$T_{\text{BeLi}} = 11.3\text{MeV}/\ln\left(1.8\frac{Y_{^9\text{Be}}/Y_{^8\text{Li}}}{Y_{^7\text{Be}}/Y_{^6\text{Li}}}\right), \quad (6)$$

the latter being deduced from Li and Be fragment yields (right panel, Ref. [28]). The apparent temperatures as given by the formulas are displayed, i.e., without corrections for secondary decays feeding the ground states of these nuclei. Secondary decays are expected to lower the apparent values by 10–20% with respect to the actual breakup temperature [27,28].

In Ref. [35], the near invariance of the measured breakup temperatures with the isotopic composition of the fragmenting system was shown to be contrary to the Hartree-Fock predictions for the limiting temperatures of excited compound nuclei [83]. Their global behavior is, on the other hand, in good qualitative agreement with the SMM calculations for ^{124}Sn and ^{124}La nuclei of Ogul and Botvina [84]. The differences obtained for these two cases are negligible in the multifragmentation regime and reach a maximum $\Delta T \approx 0.4$ MeV in the transition region where the equilibrium temperature for the more proton-rich ^{124}La system is slightly lower. As discussed in Ref. [84], the difference appears because, in the case of neutron-rich sources, partitions with a compoundlike fragment and many free neutrons are still frequent in the transition regime. Their temperature is higher than that of partitions involving a few charged fragments which are more probable for neutron-poor systems.

The ensemble calculations performed in the present work permit a more realistic comparison than those for sources with fixed mass and charge of Ref. [84]. The result, however, remains the same. As shown in Fig. 25, the dependence on N/Z of the mean microcanonical breakup temperatures, sorted according to Z_{bound}, is negligible in the regime of multifragmentation. In the most peripheral bin with large Z_{bound}, the temperature of the more neutron-rich system is slightly larger, a tendency that is also apparent in the experimental isotope temperatures (Fig. 24). The shaded band in the figure represents the full range of the apparent T_{HeLi} and T_{BeLi} temperatures, which, in the regime of multifragmentation, are close to the microscopic temperatures. These results not only

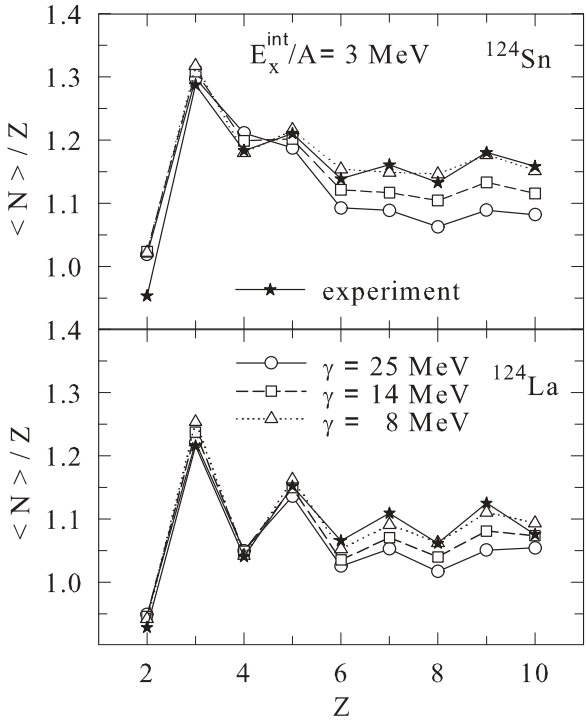

FIG. 22. Mean neutron-to-proton ratio $\langle N\rangle/Z$ of fragments produced in the fragmentation of ^{124}Sn (top panel) and ^{124}La (bottom panel) projectiles in the range $0.4 \leqslant Z_{\rm bound}/Z_0 < 0.6$. The experimental results (stars) are compared with SMM calculations using the three indicated values of the symmetry-term coefficient γ and $E_x^{\rm int} = 3$ MeV/nucleon as the start value of the interpolation interval for the secondary-decay stage of the calculations. With this choice, $\gamma = 8$ MeV (triangles) gives the best agreement with the data.

confirm the usefulness of isotope temperatures for describing properties of the chemical freeze-out stage but also suggest that the transition from compound decay to multifragmentation can be explained statistically with the opening of the fragmentation phase space [35].

The calculations were performed with the surface- and symmetry-energy parameters suggested by the analyses of the previous sections, in particular also with $\gamma = 14$ MeV. Variations of this parameter did not influence the results, however [68]. On the absolute scale, the microscopic temperature of 6.0 MeV in the center of the fragmentation regime ($\langle Z_{\rm bound}/Z_0\rangle = 0.5$) is only a few percent higher than the apparent isotope temperatures. The present calculations thus suggest less of a side-feeding correction than the up to ≈20% derived from a variety of models in Refs. [27,28]. This emphasizes once more the quantitative uncertainty inherent in estimating the effects of secondary decays but also supports the conclusion that they are relatively small for the two temperature observables chosen here. The calculations do not reproduce the accelerated rise of the apparent temperature $T_{\rm HeLi}$ at very small $Z_{\rm bound}/Z_0 \leqslant 0.2$ and are still about 1 MeV below the corresponding value of $T_{\rm BeLi}$. A contribution to the event class with very small $Z_{\rm bound}$ from collisions with more central impact parameters can explain this observation (cf. Sec. II). Isotope temperatures involving yields of carbon and oxygen isotopes have also been investigated and found

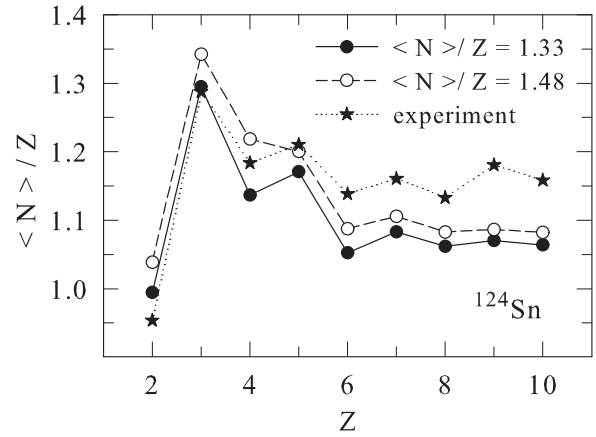

FIG. 23. Mean neutron-to-proton ratio $\langle N\rangle/Z$ of fragments with $Z \leqslant 10$ produced in the fragmentation of ^{124}Sn projectiles in the range $0.4 \leqslant Z_{\rm bound}/Z_0 < 0.6$. The experimental results (stars) are compared with SMM calculations for the nominal $N/Z = 1.48$ of that system (open circles) and for a reduced initial $N/Z = 1.33$ ratio (dots). The standard liquid-drop parameters $B_0 = 18$ and $\gamma = 25$ MeV were used.

to remain close to $T \approx 6$ MeV, practically independent of $Z_{\rm bound}$ and in good agreement with the results reported for the fragmentation of ^{197}Au projectiles [28].

C. Isoscaling and the symmetry term

Isoscaling concerns the production ratios R_{21} of fragments with neutron number N and proton number Z in reactions with different isospin asymmetry. It is defined as their exponential dependence on N and Z according to

$$R_{21}(N, Z) = Y_2(N, Z)/Y_1(N, Z) \propto \exp(N\alpha + Z\beta), \quad (7)$$

with parameters α and β. Here Y_2 and Y_1 denote the yields from the more neutron-rich and the more neutron-poor reaction system, respectively [39,85]. Isoscaling has the property that

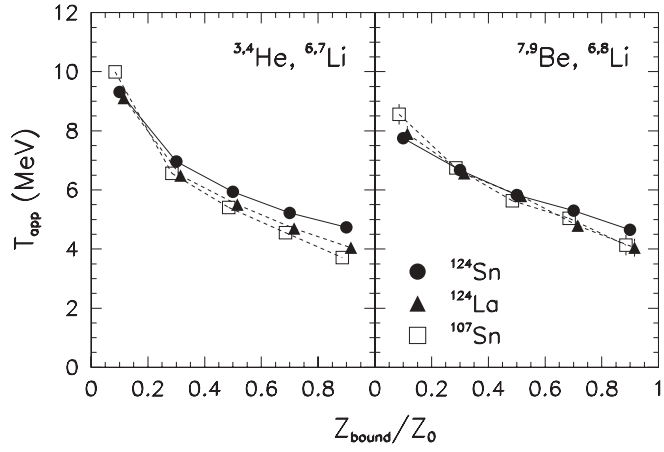

FIG. 24. Apparent temperatures $T_{\rm HeLi}$ (left panel) and $T_{\rm BeLi}$ (right panel) as a function of $Z_{\rm bound}/Z_0$ for the three reaction systems. For clarity, two of the three data sets are slightly shifted horizontally; statistical errors are displayed where they are larger than the symbol size (from Ref. [35]).

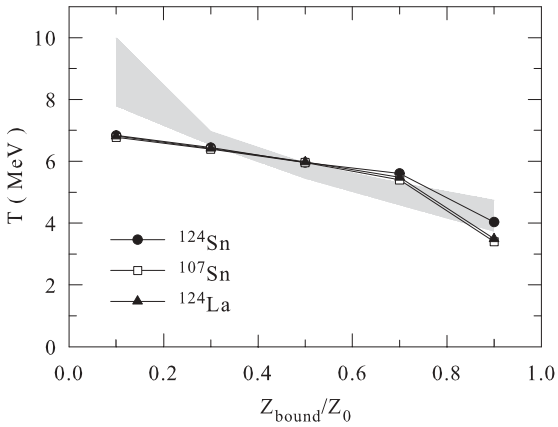

FIG. 25. Mean microcanonical temperatures calculated for the three projectile ensembles with the N/Z dependent surface coefficients $B_0 = 17.5$ and 19 MeV and with a symmetry coefficient $\gamma = 14$ MeV. The experimental result is represented by the shaded band that extends from the lowest to the highest of the six apparent T_{HeLi} and T_{BeLi} temperatures shown in Fig. 24.

a comparison is made for the same isotopes produced by different sources, so that the effects of yield fluctuations due to nuclear structure effects may be reduced.

The comparison of the measured isotope yields from the fragmentation of ^{124}Sn and of the two neutron-poor systems has confirmed that isoscaling is observed [34,86]. The isoscaling parameter α, determined from the yields for $3 \leqslant Z \leqslant 10$ in different ranges of Z_{bound}/Z_0, is shown in Fig. 26. It is seen to decrease rapidly as the disintegration of the spectator systems into fragments and light particles increases, as reported previously for the fragmentation of target spectators in reactions of ^{12}C on ^{112,124}Sn at 300 and 600 MeV/nucleon [36]. Nearly identical results are obtained for the isotopic and isobaric pairs of reactions.

In the same figure, the results obtained from SMM ensemble calculations with different symmetry-term coefficients γ and determined for $3 \leqslant Z \leqslant 10$ are compared with the data. Smaller values of γ lead to smaller isoscaling parameters α because the isotope distributions become wider and the variation of the yield ratios with N becomes correspondingly smaller. The SMM standard value $\gamma = 25$ MeV is applicable only in the bin of largest Z_{bound}. Smaller values must be chosen to reproduce the rapidly decreasing parameter α in the fragmentation regime at smaller Z_{bound}.

The proportionality expected for the dependence of α on γ is demonstrated in Fig. 27. It is fulfilled in good approximation for the hot fragments at freeze-out (open symbols in the figure). Using the calculated values of α for $\gamma = 14$ MeV and the microscopic temperature for this interval, $T = 6.0$ MeV, it is even possible to test the widely used formula

$$\alpha \approx \frac{4\gamma}{T}\left(\frac{Z_1^2}{A_1^2} - \frac{Z_2^2}{A_2^2}\right), \tag{8}$$

where Z_1,A_1 and Z_2,A_2 are the atomic and mass numbers of the two thermalized systems. The numerical factor deduced from the ensemble calculations is 3.8 while the nominal coefficient, analytically derived in the zero-temperature limit, is 4 [39].

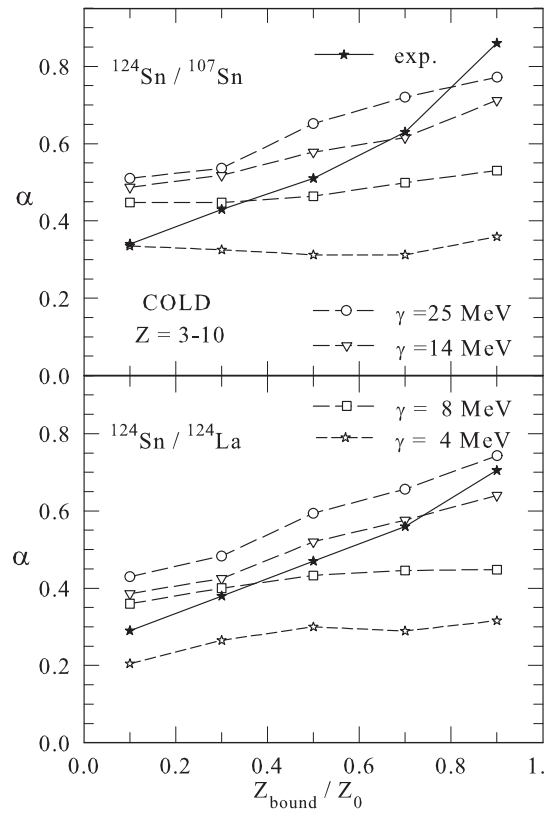

FIG. 26. Experimental data (stars) and SMM ensemble calculations (open symbols) of isoscaling coefficients α extracted from fragment yield ratios ($3 \leqslant Z \leqslant 10$) for ^{124}Sn and ^{107}Sn projectiles (top panel) and for ^{124}Sn and ^{124}La projectiles (bottom panel) as a function of the reduced bound charge Z_{bound}/Z_0. Four different symmetry-term coefficients γ were used in the SMM calculations as indicated.

The validity of Eq. (8) at finite temperatures has recently also been confirmed by Souza *et al.* [87] in a theoretical study with the SMM.

This relation was independently deduced from dynamical and statistical investigations [39,88,89] and used in several analyses of experiments [36,66,67,90]. The SMM ensemble calculations show that, within some approximation, this relation remains valid for the cold fragment yields as long as γ is close to its conventional value of 25 MeV. As γ is lowered the resulting α for the asymptotic fragments becomes larger and deviates increasingly from the value for hot fragments (Fig. 27). During the late stages of the secondary decays, the available daughter states are increasingly concentrated in the valley of stability, which narrows the initially wide isotope distributions. This effect has been demonstrated already and discussed in Ref. [36].

D. The role of the surface

The symmetry-term coefficient γ resulting from the isoscaling analysis is shown in Fig. 28 (dots) as a function of the sorting variable Z_{bound}. For large $Z_{bound}/Z_0 > 0.8$, the experimental values of α for the isotopic and isobaric pairs of reactions differ (Fig. 26), but the prediction for $\gamma = 25$ MeV

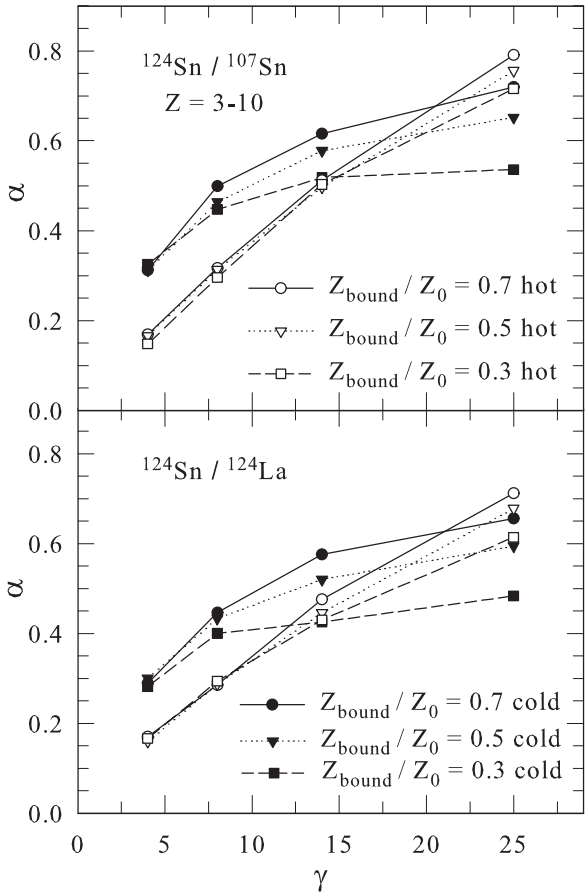

FIG. 27. Theoretical isoscaling coefficients α calculated for three intervals in Z_{bound}/Z_0 and for both hot primary fragments (open symbols, legend in upper panel) and cold fragments after secondary deexcitation (closed symbols, legend in lower panel).

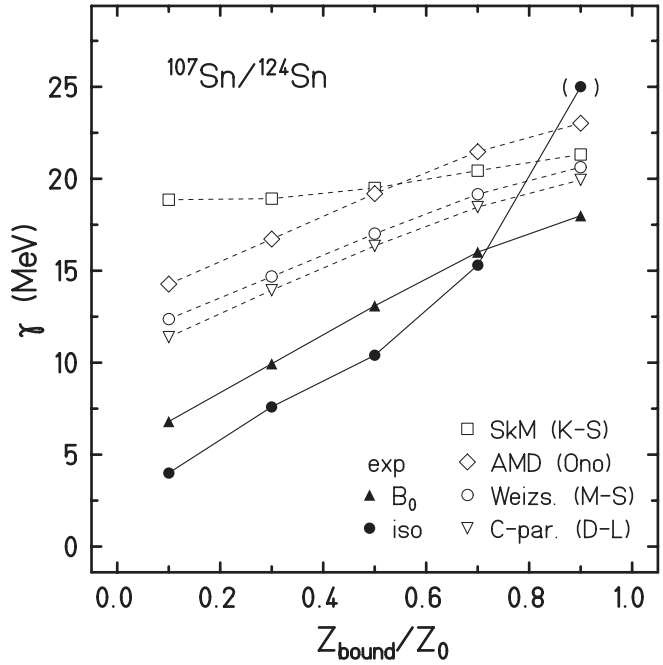

FIG. 28. Effective symmetry-term coefficient γ as expected from the changing fragment-mass distributions using surface and volume symmetry-term coefficients from Refs. [65,75,93,94] (open diamonds, circles, triangles, and squares, respectively) in comparison with the coefficient γ for hot fragments obtained with the SMM from the N/Z dependence of B_0 (solid triangles) and from the isoscaling analysis for the ^{107,124}Sn pair of reactions (dots).

is close to the mean. The rapid drop for smaller Z_{bound} is consistently evident from the two data sets (Fig. 26). For comparison, four predictions are shown in Fig. 28, obtained with rather different approaches but all containing the effect of the surface-symmetry term whose importance increases for the lower-mass fragments [91]. The coefficients of the mass formula of Myers and Swiatecki [75] are adapted to ground-state masses, and values close to them have been used in other studies [92]. From the energies of isobaric analog states, a relation between the volume and surface capacitances of nuclei for absorbing asymmetry $N - Z$ was derived by Danielewicz and Lee [93], while Kolomietz and Sanzhur [94] have used a variational approach using Skyrme forces to derive equilibrium values for the volume symmetry term with surface and curvature corrections for nuclei along the β-stability line. Theoretical surface and volume terms were also obtained by Ono *et al.* [65] from fitting the ground-state binding energies calculated with the antisymmetrized molecular dynamics (AMD) model.

With these parametrizations, an effective symmetry energy averaged over the set of partitions was calculated for the five bins in Z_{bound} after the experimental Z distributions had been converted to mass distributions using the projectile N/Z. The obtained results show similar trends. The smaller fragments produced at higher excitations cause the effective mean symmetry term to decrease with decreasing Z_{bound} in all four cases, but at a slower rate than that resulting from the isoscaling analysis of the experimental yield ratios.

The same procedure was, in addition, also performed with the surface-symmetry coefficient $\gamma_s = 45$ MeV derived from the N/Z dependence of the surface-term coefficient B_0 (Sec. IV), combined with the volume-symmetry coefficient $\gamma_v = 28$ MeV of the mass formula of Myers and Swiatecki [75]. As expected, the drop with decreasing Z_{bound} is faster because of the larger surface-symmetry coefficient and close to that deduced from the isoscaling analysis. Within their larger uncertainty, the conclusions drawn from the analysis of the charge observables are thus consistent with those obtained from the isoscaling analysis of the measured isotope distributions. Increased surface effects are expected if deformations and exotic shapes are present among the smaller fragments at the chemical freeze-out.

The symmetry-term coefficients of the AMD ground-state nuclei follow the trend exhibited by the other mass formulas. However, for excited nuclei at the breakup stage, a reduced volume term and an isospin-independent surface term for the larger IMFs were found in the AMD study [65]. From this result and from the τ analysis of fragment-charge yields [74] one may conclude that the strong decrease of γ with decreasing Z_{bound} is unlikely to result from a surface effect alone. In fact, the surface term should decrease also for fragments in close vicinity of other nuclei because of residual interactions. The

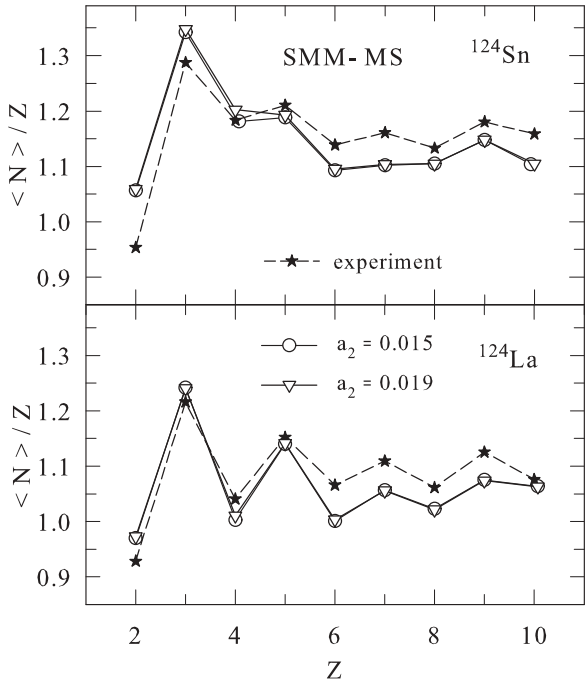

FIG. 29. Mean neutron-to-proton ratio $\langle N\rangle/Z$ of fragments with $Z \leqslant 10$ produced in the fragmentation of ^{124}Sn (top panel) and ^{124}La (bottom panel) projectiles in the range $0.4 \leqslant Z_{\rm bound}/Z_0 < 0.6$. The experimental results (stars) are compared with SMM calculations with the Myers-Swiatecki parametrization [75] for the liquid-drop description of fragments and for two ensembles as indicated (open symbols).

reduced symmetry term will then have to originate from a decrease of the overall matter density caused by the expansion of the system [69,95] and leading to expanded or deformed shapes of fragments as they are produced. These effects should be considered in the AMD model but were, perhaps, not tested over the full range of possible excitations in Ref. [65]. There, the temperature at breakup was estimated to be less than 4 MeV, which corresponds to the bin of largest $Z_{\rm bound}$ here (Fig. 24) for which the deduced γ is comparable to the AMD result. The stronger reduction is observed at the higher temperatures at smaller $Z_{\rm bound}$ (Fig. 28).

On the quantitative level, different degrees of reduction are deduced with the different methods. The lowest values for γ are obtained from the isoscaling analysis. The $\gamma \approx$ 10 MeV obtained for the center of the fragmentation regime, i.e., $Z_{\rm bound}/Z_0 \approx 0.5$, is to be compared to 13 MeV, corresponding to $\Delta B_0 = 1.5$ MeV but carrying a large uncertainty, and to $\gamma = 14$ MeV which provided the best global agreement with the charge and isotope observables studied in Secs. IV and V. An answer may come from the fact that isoscaling is more sensitive to the widths of the isotope distributions and thus may give a larger weight to their tails. These quantities, on the other hand, may more strongly depend on the realization chosen for the secondary decay stage of the reaction. As discussed above, values below 14 MeV are favored by the odd-even structure of $\langle N\rangle/Z$ for $Z \geqslant 6$ (Fig. 22).

The global $\gamma = 14$ MeV seems close to the effective coefficient $\gamma = 17$ MeV obtained from the parametrizations of Myers and Swiatecki or Danielewicz and Lee, including only surface effects of isolated nuclei (Fig. 28). However, the difference is significant. SMM calculations using the coefficients of Myers and Swiatecki for the fragment description throughout, i.e., at breakup as well as during the secondary decay stages, lead to significantly smaller $\langle N\rangle/Z$, as shown for the ^{124}Sn and ^{124}La systems in Fig. 29. They are not sufficient to reproduce the observed neutron richness of light fragments. When searching for possible reasons for these large differences it was found that the reduction of γ lowers the Q value for proton emission while this is not the case with the Myers-Swiatecki parameters. The relative probability for proton emission is thus enhanced, leading to more neutron-rich daughter nuclei.

VII. CONCLUSIONS

New results from a systematic study of the N/Z dependence of projectile fragmentation at an incident energy of 600 MeV/nucleon have been presented. By employing radioactive secondary beams, a large range of isotopic compositions has been explored, up to the present technical limit. Global fragmentation observables were found to depend weakly on the projectile N/Z while substantial differences are observed for the isotope distributions of light fragments ($Z \leqslant 10$).

The significance of the measured charge and mass yields and correlations was investigated with the SMM by performing ensemble calculations accounting for the mass-energy correlation of the produced spectator nuclei. The ensemble parameters were determined empirically by searching for an optimum reproduction of the measured fragment Z yields and correlations. The sensitivity of the liquid-drop parameters of the fragment description in the hot freeze-out environment was studied and, as a main result, a significant reduction of the symmetry-term coefficient γ was found necessary to reproduce the mean neutron-to-proton ratios $\langle N\rangle/Z$ and the isoscaling parameters of $Z \leqslant 10$ fragments. With $\gamma =$ 14 MeV a globally good reproduction was obtained while even lower values are suggested by some observations. Studied as a function of the impact parameter, γ is found to decrease rapidly as the multiplicity of fragments and light particles from the disintegration of the produced spectator systems increases. The reduction is larger than that expected from the decreasing fragment size and the correspondingly larger surface effects as modeled with standard mass formulas. It is interpreted as resulting from the overall reduced density of the system at breakup and the modified fragment properties in the hot environment. Deformations and reduced fragment densities at chemical freeze-out contribute to producing the observed yields of neutron-rich fragments which, according to the present investigation with the SMM, are particularly sensitive to the widths of the isotope distributions and thus to the symmetry-energy term at freeze-out.

The reproduction of the experimental data with the SMM ensemble calculations is found to be very satisfactory. A global normalization on the level of the $Z_{\rm bound}$-sorted event distributions was found sufficient for reaching an overall quantitative description of the Z and A resolved fragment

yields. The calculations have, therefore, also been used to address open questions regarding the isotopic compositions and temperatures of the system at the freeze-out stage. The N/Z independence of the breakup temperatures in the fragmentation regime, obtained from double-isotope yields of light fragments, is quantitatively reproduced by the microscopic SMM temperature. The good agreement suggests that the opening phase space is sufficient to initiate the transition from predominantly residue formation to multifragment breakups as the transferred energy increases. Changes of the isotopic evolution of the spectator system between its formation during the initial nucleon-nucleon cascades and its subsequent breakup have been ruled out as alternative explanations for the isotopic fragment compositions. A reduced difference of the system N/Z at breakup will result in smaller isoscaling parameters but, at the same time, require even larger reductions of the symmetry-term coefficient in order to reproduce the mean $\langle N\rangle/Z$ of intermediate-mass fragments.

It is finally emphasized that the simultaneous analysis of several observables obtained from a nearly complete coverage of the spectator kinematic regime has been important for reaching the presented conclusions. The deduced modifications of hot fragments in the low-density freeze-out environment and in the presence of other fragments and nuclei can be expected to influence the modeling of astrophysical processes.

ACKNOWLEDGMENTS

The authors gratefully acknowledge the contributions of the GSI accelerator division in providing high-intensity and high-quality ^{124}Sn and ^{142}Nd beams and technical support. R.O. thanks TUBITAK and DFG for financial support. A.S.B. is grateful to FIAS, Frankfurt; the GSI Helmholtzzentrum, Darmstadt; and the IKP of Mainz University for support and hospitality. C.Sf. acknowledges support by the Alexander-von-Humboldt Foundation. This work has been supported by the European Community under Contract No. HPRI-CT-1999-00001 and by the Polish Ministry of Science and Higher Education under Contracts No. 1 P03B 105 28 (2005–2006) and No. N202 160 32/4308 (2007–2009), and it has been partly supported by Grants NS-7235.2010.2 and RFBR 09-02-91331 (Russia).

[1] D. H. E. Gross, Rep. Prog. Phys. **53**, 605 (1990).
[2] J. P. Bondorf, A. S. Botvina, A. S. Iljinov, I. N. Mishustin, and K. Sneppen, Phys. Rep. **257**, 133 (1995).
[3] *Dynamics and Thermodynamics with Nuclear Degrees of Freedom*, edited by Ph. Chomaz, F. Gulminelli, W. Trautmann, and S. J. Yennello (Springer, Berlin/Heidelberg/New York, 2006); Eur. Phys. J. A **30**, 1 (2006).
[4] V. E. Viola *et al.*, Phys. Rep. **434**, 1 (2006).
[5] N. Bohr, Nature (London) **137**, 344 (1936).
[6] G. Bertsch and P. J. Siemens, Phys. Lett. B **126**, 9 (1983).
[7] J. Desbois, R. Boisgard, C. Ngô, and J. Nemeth, Z. Phys. A **328**, 101 (1987).
[8] W. A. Friedman, Phys. Rev. C **42**, 667 (1990).
[9] L. Beaulieu *et al.*, Phys. Rev. Lett. **84**, 5971 (2000).
[10] V. Karnaukhov *et al.*, Phys. At. Nucl. **66**, 1242 (2003).
[11] Y. K. Vermani and R. K. Puri, Europhys. Lett. **85**, 62001 (2009).
[12] H. Xi *et al.*, Z. Phys. A **359**, 397 (1997); H. Xi, Eur. Phys. J. A **1**, 235 (1998).
[13] A. S. Botvina, A. S. Iljinov, and I. N. Mishustin, Nucl. Phys. A **507**, 649 (1990).
[14] A. S. Botvina *et al.*, Nucl. Phys. A **584**, 737 (1995).
[15] M. D'Agostino *et al.*, Phys. Lett. B **371**, 175 (1996).
[16] M. D'Agostino *et al.*, Nucl. Phys. A **650**, 329 (1999).
[17] R. P. Scharenberg *et al.*, Phys. Rev. C **64**, 054602 (2001).
[18] N. Bellaize *et al.*, Nucl. Phys. A **709**, 367 (2002).
[19] S. P. Avdeyev *et al.*, Nucl. Phys. A **709**, 392 (2002).
[20] C. Ishizuka, A. Ohnishi, and K. Sumiyoshi, Nucl. Phys. A **723**, 517 (2003).
[21] A. S. Botvina and I. N. Mishustin, Phys. Lett. B **584**, 233 (2004); Nucl. Phys. A **843**, 98 (2010).
[22] A. S. Botvina and I. N. Mishustin, Phys. Rev. C **72**, 048801 (2005).
[23] P. Kreutz *et al.*, Nucl. Phys. A **556**, 672 (1993).
[24] A. Schüttauf *et al.*, Nucl. Phys. A **607**, 457 (1996).
[25] C. A. Ogilvie *et al.*, Phys. Rev. Lett. **67**, 1214 (1991).
[26] J. Hubele *et al.*, Z. Phys. A **340**, 263 (1991).
[27] J. Pochodzalla *et al.*, Phys. Rev. Lett. **75**, 1040 (1995).
[28] W. Trautmann *et al.*, Phys. Rev. C **76**, 064606 (2007).
[29] J. Bondorf, R. Donangelo, I. N. Mishustin, and H. Schulz, Nucl. Phys. A **444**, 460 (1985).
[30] X. Campi, Phys. Lett. B **208**, 351 (1988).
[31] F. Gulminelli and M. D'Agostino, Eur. Phys. J. A **30**, 253 (2006).
[32] G. Chaudhuri and S. Das Gupta, Phys. Rev. C **75**, 034603 (2007).
[33] C. Sfienti *et al.*, Nucl. Phys. A **749**, 83c (2005).
[34] W. Trautmann *et al.*, Int. J. Mod. Phys. E **17**, 1838 (2008).
[35] C. Sfienti *et al.*, Phys. Rev. Lett. **102**, 152701 (2009).
[36] A. Le Fèvre *et al.*, Phys. Rev. Lett. **94**, 162701 (2005).
[37] H. Geissel *et al.*, Nucl. Instrum. Methods B **70**, 286 (1992).
[38] J. Łukasik *et al.*, Nucl. Instrum. Methods A **587**, 413 (2008).
[39] A. S. Botvina, O. V. Lozhkin, and W. Trautmann, Phys. Rev. C **65**, 044610 (2002).
[40] C. Sfienti *et al.*, in *Proceedings of the XLIst International Winter Meeting on Nuclear Physics, Bormio, Italy*, edited by I. Iori and A. Moroni (Ricerca Scientifica ed Educazione Permanente Suppl. No. 120, Milano, 2003), p. 323.
[41] Th. Rubehn *et al.*, Phys. Rev. C **53**, 993 (1996).
[42] M. Begemann-Blaich *et al.*, Phys. Rev. C **58**, 1639 (1998).
[43] J. Gosset, H. H. Gutbrod, W. G. Meyer, A. M. Poskanzer, A. Sandoval, R. Stock, and G. D. Westfall, Phys. Rev. C **16**, 629 (1977).
[44] A. S. Botvina, K. K. Gudima, A. S. Iljinov, and I. N. Mishustin, Phys. At. Nucl. **57**, 628 (1994).
[45] E. Le Gentil *et al.*, Phys. Rev. Lett. **100**, 022701 (2008).
[46] T. Gaitanos, H. Lenske, and U. Mosel, Phys. Lett. B **675**, 297 (2009).
[47] H. W. Barz, W. Bauer, J. P. Bondorf, A. S. Botvina, R. Donangelo, H. Schulz, and K. Sneppen, Nucl. Phys. A **561**, 466 (1993).
[48] A. H. Raduta, M. Colonna, and M. Di Toro, Phys. Rev. C **76**, 024602 (2007).
[49] A. S. Botvina and I. N. Mishustin, Phys. Lett. B **294**, 23 (1992).

[50] B.-A. Li, A. R. DeAngelis, and D. H. E. Gross, Phys. Lett. B **303**, 225 (1993).
[51] P. Désesquelles, A. Lleres, M. Charvet, A. J. Cole, A. Giorni, D. Heuer, and J. B. Viano, Phys. Rev. C **53**, 2252 (1996).
[52] Al. H. Raduta and Ad. R. Raduta, Phys. Rev. C **61**, 034611 (2000).
[53] A. Le Fèvre *et al.*, Nucl. Phys. A **735**, 219 (2004).
[54] T. Odeh *et al.*, Phys. Rev. Lett. **84**, 4557 (2000).
[55] S. Das Gupta and A. Z. Mekjian, Phys. Rev. C **57**, 1361 (1998).
[56] K. A. Bugaev, M. I. Gorenstein, I. N. Mishustin, and W. Greiner, Phys. Lett. B **498**, 144 (2001).
[57] G. Chaudhuri and S. Das Gupta, Phys. Rev. C **80**, 044609 (2009).
[58] A. S. Botvina and I. N. Mishustin, Phys. Rev. C **63**, 061601(R) (2001).
[59] A. S. Botvina, A. S. Iljinov, and I. N. Mishustin, Sov. J. Nucl. Phys. **42**, 712 (1985).
[60] S. Fritz *et al.*, Phys. Lett. B **461**, 315 (1999).
[61] V. E. Viola, K. Kwiatkowski, J. B. Natowitz, and S. J. Yennello, Phys. Rev. Lett. **93**, 132701 (2004).
[62] A. S. Botvina, A. S. Iljinov, I. N. Mishustin, J. P. Bondorf, R. Donangelo, and K. Sneppen, Nucl. Phys. A **475**, 663 (1987).
[63] A. S. Botvina, A. B. Larionov, and I. N. Mishustin, Phys. At. Nucl. **58**, 1703 (1995).
[64] V. Baran, M. Colonna, M. Di Toro, V. Greco, M. Zielinska-Pfabé, and H. H. Wolter, Nucl. Phys. A **703**, 603 (2002).
[65] A. Ono, P. Danielewicz, W. A. Friedman, W. G. Lynch, and M. B. Tsang, Phys. Rev. C **70**, 041604(R) (2004).
[66] J. Iglio, D. V. Shetty, S. J. Yennello, G. A. Souliotis, M. Jandel, A. L. Keksis, S. N. Soisson, B. C. Stein, S. Wuenschel, and A. S. Botvina, Phys. Rev. C **74**, 024605 (2006).
[67] G. A. Souliotis, A. S. Botvina, D. V. Shetty, A. L. Keksis, M. Jandel, M. Veselsky, and S. J. Yennello, Phys. Rev. C **75**, 011601(R) (2007).
[68] N. Buyukcizmeci, R. Ogul, and A. S. Botvina, Eur. Phys. J. A **25**, 57 (2005).
[69] N. Buyukcizmeci, A. S. Botvina, I. N. Mishustin, and R. Ogul, Phys. Rev. C **77**, 034608 (2008).
[70] S. Typel, G. Röpke, T. Klähn, D. Blaschke, and H. H. Wolter, Phys. Rev. C **81**, 015803 (2010).
[71] J. B. Natowitz *et al.*, Phys. Rev. Lett. **104**, 202501 (2010).
[72] J. A. Hauger *et al.*, Phys. Rev. C **62**, 024616 (2000).
[73] J. Hubele *et al.*, Phys. Rev. C **46**, R1577 (1992).
[74] A. S. Botvina, N. Buyukcizmeci, M. Erdogan, J. Lukasik, I. N. Mishustin, R. Ogul, and W. Trautmann, Phys. Rev. C **74**, 044609 (2006).
[75] W. D. Myers and W. J. Swiatecki, Nucl. Phys. **81**, 1 (1966).
[76] R. Ogul, U. Atav, F. Bulut, N. Buyukcizmeci, M. Erdogan, H. Imal, A. S. Botvina, and I. N. Mishustin, J. Phys. G **36**, 115106 (2009).
[77] W. Trautmann, Nucl. Phys. A **787**, 575c (2007).
[78] E. M. Winchester *et al.*, Phys. Rev. C **63**, 014601 (2000).
[79] M. V. Ricciardi *et al.*, Nucl. Phys. A **733**, 299 (2004).
[80] S. Hudan *et al.*, Phys. Rev. C **80**, 064611 (2009).
[81] D. Henzlova *et al.*, J. Phys. G **37**, 085010 (2010).
[82] M. B. Tsang *et al.*, Phys. Rev. Lett. **92**, 062701 (2004).
[83] J. Besprosvany and S. Levit, Phys. Lett. B **217**, 1 (1989).
[84] R. Ogul and A. S. Botvina, Phys. Rev. C **66**, 051601(R) (2002).
[85] M. B. Tsang, W. A. Friedman, C. K. Gelbke, W. G. Lynch, G. Verde, and H. Xu, Phys. Rev. Lett. **86**, 5023 (2001).
[86] S. Bianchin *et al.*, in *Proceedings of the XLVth International Winter Meeting on Nuclear Physics, Bormio, Italy*, edited by I. Iori and A. Tarantola (Ricerca Scientifica ed Educazione Permanente Suppl. No. 127, Milano, 2007), p. 233.
[87] S. R. Souza, M. B. Tsang, B. V. Carlson, R. Donangelo, W. G. Lynch, and A. W. Steiner, Phys. Rev. C **80**, 044606 (2009).
[88] M. B. Tsang *et al.*, Phys. Rev. C **64**, 054615 (2001).
[89] A. Ono, P. Danielewicz, W. A. Friedman, W. G. Lynch, and M. B. Tsang, Phys. Rev. C **68**, 051601(R) (2003).
[90] S. Kowalski *et al.*, Phys. Rev. C **75**, 014601 (2007).
[91] S. R. Souza, M. B. Tsang, R. Donangelo, W. G. Lynch, and A. W. Steiner, Phys. Rev. C **78**, 014605 (2008).
[92] Ad. R. Raduta and F. Gulminelli, Phys. Rev. C **75**, 024605 (2007).
[93] P. Danielewicz and J. Lee, Int. J. Mod. Phys. E **18**, 892 (2009).
[94] V. M. Kolomietz and A. I. Sanzhur, Eur. Phys. J. A **38**, 345 (2008).
[95] B.-A. Li and L.-W. Chen, Phys. Rev. C **74**, 034610 (2006).